

STATE OF THE CLIMATE IN 2020

ANTARCTICA AND THE SOUTHERN OCEAN

S. Stammerjohn and T. Scambos, Eds.



Special Online Supplement to the *Bulletin of the American Meteorological Society* Vol.102, No. 8, August, 2021

<https://doi.org/10.1175/BAMS-D-21-0081.1>

Corresponding author: Sharon Stammerjohn / Sharon.Stammerjohn@colorado.edu

©2021 American Meteorological Society

For information regarding reuse of this content and general copyright information, consult the [AMS Copyright Policy](#).

STATE OF THE CLIMATE IN 2020

Antarctica and the Southern Ocean

Editors

Jessica Blunden
Tim Boyer

Chapter Editors

Freya Aldred
Peter Bissolli
Howard J. Diamond
Matthew L. Druckenmiller
Robert J. H. Dunn
Catherine Ganter
Nadine Gobron
Gregory C. Johnson
Tim Li
Rick Lumpkin
Ademe Mekonnen
John B. Miller
Twila A. Moon
Ahira Sánchez-Lugo
Ted A. Scambos
Carl J. Schreck III
Sharon Stammerjohn
Richard L. Thoman
Kate M. Willett

Technical Editor

Andrea Andersen

BAMS Special Editor for Climate

Michael A. Alexander

American Meteorological Society

Cover credit:

Scientists acquiring measurements of East Antarctic sea ice and snow cover thickness and properties during the 2003 Australian-led ARISE multi-disciplinary field experiment. The photo was taken by Rob Massom (Australian Antarctic Division) on 10 October 2003.

Antarctica and the Southern Ocean is one chapter from the *State of the Climate in 2020* annual report and is available from <https://doi.org/10.1175/BAMS-D-21-0081.1>. Compiled by NOAA's National Centers for Environmental Information, *State of the Climate in 2020* is based on contributions from scientists from around the world. It provides a detailed update on global climate indicators, notable weather events, and other data collected by environmental monitoring stations and instruments located on land, water, ice, and in space. The full report is available from <https://doi.org/10.1175/2021BAMSSStateoftheClimate.1>.

How to cite this document:**Citing the complete report:**

Blunden, J. and T. Boyer, Eds., 2021: "State of the Climate in 2020". *Bull. Amer. Meteor. Soc.*, **102** (8), S1–S475, <https://doi.org/10.1175/2021BAMSSStateoftheClimate.1>

Citing this chapter:

Stammerjohn, S. and T. Scambos, Eds., 2021: Antarctica and the Southern Ocean [in "State of the Climate in 2020"]. *Bull. Amer. Meteor. Soc.*, **102** (8), S317–S355, <https://doi.org/10.1175/BAMS-D-21-0081.1>.

Citing a section (example):

Kramarova, N., P. A. Newman, E. R. Nash, S. E. Strahan, C. S. Long, B. Johnson, M. Pitts, M. L. Santee, I. Petropavlovskikh, L. Coy, J. de Laat, G. H. Bernhard, S. Stierle, and K. Lakkala, 2021: 2020 Antarctic ozone hole [in "State of the Climate in 2020"]. *Bull. Amer. Meteor. Soc.*, **102** (8), S345–S349, <https://doi.org/10.1175/BAMS-D-21-0081.1>.

Editor and Author Affiliations (alphabetical by name)

- Adusumilli, Susheel**, Scripps Institution of Oceanography, University of California San Diego, La Jolla, California
- Barreira, Sandra**, Argentine Naval Hydrographic Service, Buenos Aires, Argentina
- Bernhard, Germar H.**, Biospherical Instruments Inc., San Diego, California
- Bozkurt, Deniz**, Department of Meteorology, University of Valparaíso, Valparaíso and Center for Climate and Resilience Research (CR)2, Santiago, Chile
- Bushinsky, Seth M.**, University of Hawaii at Mānoa, Honolulu, Hawaii
- Clem, Kyle R.**, School of Geography, Environment and Earth Sciences, Victoria University of Wellington, Wellington, New Zealand
- Colwell, Steve**, British Antarctic Survey, Cambridge, United Kingdom
- Coy, Lawrence**, Science Systems and Applications, Inc., NASA Goddard Space Flight Center, Greenbelt, Maryland
- De Laat, Jos**, Royal Netherlands Meteorological Institute (KNMI), DeBilt, Netherlands
- du Plessis, Marcel D.**, Department of Marine Sciences, University of Gothenburg, Gothenburg, Sweden
- Fogt, Ryan L.**, Department of Geography, Ohio University, Athens, Ohio
- Foppert, Annie**, Australian Antarctic Program Partnership, Hobart, Tasmania, Australia
- Fricker, Helen Amanda**, Scripps Institution of Oceanography, University of California San Diego, La Jolla, California
- Gardner, Alex S.**, Jet Propulsion Laboratory, California Institute of Technology, Pasadena, California
- Gille, Sarah T.**, Climate, Atmospheric Science and Physical Oceanography, Scripps Institution of Oceanography, University of California, San Diego, La Jolla, California
- Gorte, Tessa**, Department of Atmospheric and Oceanic Sciences, University of Colorado Boulder, Boulder, Colorado
- Johnson, Bryan**, NOAA/OAR Earth System Research Laboratory, Global Monitoring Division, and University of Colorado, Boulder, Colorado
- Keenan, Eric**, Department of Atmospheric and Oceanic Sciences, University of Colorado Boulder, Boulder, Colorado
- Kennett, Daemon**, School of Geography, Environment and Earth Sciences, Victoria University of Wellington, Wellington, New Zealand
- Keller, Linda M.**, Department of Atmospheric and Oceanic Sciences, University of Wisconsin-Madison, Madison, Wisconsin
- Kramarova, Natalya A.**, NASA Goddard Space Flight Center, Greenbelt, Maryland
- Lakkala, Kaisa**, Finnish Meteorological Institute, Helsinki, Finland
- Lazzara, Matthew A.**, Department of Physical Sciences, School of Arts and Sciences, Madison Area Technical College, and Space Science and Engineering Center, University of Wisconsin-Madison, Madison, Wisconsin
- Lenaerts, Jan T. M.**, Department of Atmospheric and Oceanic Sciences, University of Colorado Boulder, Boulder, Colorado
- Lieser, Jan L.**, Australian Bureau of Meteorology, Hobart, TAS, Australia, and Institute for Marine and Antarctic Studies, University of Tasmania, Hobart, Tasmania, Australia
- Li, Zhi**, Climate Change Research Centre, University of New South Wales, Sydney, New South Wales, Australia
- Liu, Hongxing**, Department of Geography, University of Cincinnati, Cincinnati, Ohio
- Long, Craig S.**, NOAA/NWS National Center for Environmental Prediction, College Park, Maryland
- MacFerrin, Michael**, Earth Science and Observation Center, CIRES, University of Colorado, Boulder, Colorado
- MacLennan, Michelle L.**, Department of Atmospheric and Oceanic Sciences, University of Colorado Boulder, Boulder, Colorado
- Massom, Robert A.**, Australian Antarctic Division and Australian Antarctic Program Partnership (AAPP), Hobart, Tasmania, Australia
- Mikolajczyk, David**, Space Science and Engineering Center, University of Wisconsin-Madison, Madison, Wisconsin
- Montgomery, Lynn**, Department of Atmospheric and Oceanic Sciences, University of Colorado Boulder, Boulder, Colorado
- Mote, Thomas L.**, Department of Geography, University of Georgia
- Nash, Eric R.**, Science Systems and Applications, Inc.; NASA Goddard Space Flight Center, Greenbelt, Maryland
- Newman, Paul A.**, NASA Goddard Space Flight Center, Greenbelt, Maryland
- Petropavlovskikh, Irina**, Cooperative Institute for Research in Environmental Sciences, University of Colorado Boulder, and NOAA/OAR Earth System Research Laboratory, Boulder, Colorado
- Pitts, Michael**, NASA Langley Research Center, Hampton, Virginia
- Reid, Phillip**, Australian Bureau of Meteorology and Australian Antarctic Program Partnership (AAPP), Hobart, Tasmania, Australia
- Rintoul, Steven R.**, CSIRO Oceans and Atmosphere, Hobart, Tasmania, Australia, Centre for Southern Hemisphere Oceans Research, Hobart, Tasmania, Australia, Australian Antarctic Program Partnership, Hobart, Tasmania, Australia
- Santee, Michelle L.**, NASA Jet Propulsion Laboratory, California Institute of Technology, Pasadena, California
- Scambos, Ted A.**, Earth Science and Observation Center, CIRES, University of Colorado, Boulder, Colorado
- Shadwick, Elizabeth H.**, CSIRO Oceans & Atmosphere, Hobart, Tasmania, Australia, Centre for Southern Hemisphere Oceans Research, Hobart, Tasmania, Australia, Australian Antarctic Program Partnership, Hobart, Tasmania, Australia
- Silvano, Alessandro**, Ocean and Earth Science, National Oceanography Centre, University of Southampton, Southampton, United Kingdom
- Stammerjohn, Sharon**, Institute of Arctic and Alpine Research, University of Colorado, Boulder, Colorado
- Stierle, Scott**, NOAA/OAR Global Monitoring Laboratory, Boulder, Colorado; CIRES, University of Colorado, Boulder, Colorado
- Strahan, Susan**, Universities Space Research Association, NASA Goddard Space Flight Center, Greenbelt, Maryland
- Sutton, Adrienne J.**, Pacific Marine Environmental Laboratory, NOAA, Seattle Washington
- Swart, Sebastiaan**, Department of Marine Sciences, University of Gothenburg, Gothenburg, Sweden, and Department of Oceanography, University of Cape Town, Rondebosch, South Africa
- Tamsitt, Veronica**, Climate Change Research Centre, University of New South Wales, Sydney, NSW, Australia, and Centre for Southern Hemisphere Oceans Research, Hobart, Tasmania, Australia; College of Marine Science, University of South Florida, St. Petersburg, Florida
- Tilbrook, Bronte**, CSIRO Oceans & Atmosphere, Hobart, Tasmania, Australia, and Australian Antarctic Program Partnership, Hobart, Tasmania, Australia
- Wang, Lei**, Department of Geography and Anthropology, Louisiana State University, Baton Rouge, Louisiana
- Williams, Nancy L.**, College of Marine Science, University of South Florida, St. Petersburg, Florida
- Yuan, Xiaojun**, Lamont-Doherty Earth Observatory of Columbia University, Palisades, New York

Editorial and Production Team

Allen, Jessica, Graphics Support, Cooperative Institute for Satellite Earth System Studies, North Carolina State University, Asheville, North Carolina

Andersen, Andrea, Technical Editor, Innovative Consulting Management Services, LLC, NOAA/NESDIS National Centers for Environmental Information, Asheville, North Carolina

Hammer, Gregory, Content Team Lead, Communications and Outreach, NOAA/NESDIS National Centers for Environmental Information, Asheville, North Carolina

Love-Brotak, S. Elizabeth, Lead Graphics Production, NOAA/NESDIS National Centers for Environmental Information, Asheville, North Carolina

Misch, Deborah J., Graphics Support, Innovative Consulting Management Services, LLC, NOAA/NESDIS National Centers for Environmental Information, Asheville, North Carolina

Riddle, Deborah B., Graphics Support, NOAA/NESDIS National Centers for Environmental Information, Asheville, North Carolina

Veasey, Sara W., Visual Communications Team Lead, Communications and Outreach, NOAA/NESDIS National Centers for Environmental Information, Asheville, North Carolina

6. Table of Contents

List of authors and affiliations	S320
a. Overview	S323
b. Atmospheric circulation and surface observations	S324
Sidebar 6.1: Record warmth and surface melt on the Antarctic Peninsula in February 2020.....	S328
c. Ice sheet surface mass balance	S330
d. Ice sheet seasonal melt extent and duration	S331
e. Ice sheet changes from satellite observations	S334
f. Sea ice extent, concentration, and seasonality	S336
Sidebar 6.2: “Disruption events” and large shifts in sea ice anomalies: a tropical–high latitude tango	S339
g. Southern Ocean	S341
1. Air–sea heat flux	S341
2. Mixed layer properties.....	S343
3. Air–sea CO ₂ flux.....	S343
4. Recent recovery of Antarctic Bottom Water formation.....	S345
h. 2020 Antarctic ozone hole	S345
Acknowledgments	S350
Appendix 1: Chapter - 6 Acronyms	S351
References	S352

*Please refer to Chapter 8 (Relevant datasets and sources) for a list of all climate variables and datasets used in this chapter for analyses, along with their websites for more information and access to the data.

6. ANTARCTICA AND THE SOUTHERN OCEAN

S. Stammerjohn and T. Scambos, Eds.

a. Overview—S. Stammerjohn and T. Scambos

Antarctic and Southern Ocean climate for 2020 was marked by several mid-year shifts, including reversals from generally warmer to cooler temperatures on the continent, weaker to stronger westerlies over the ocean, greater to lesser precipitation on the West Antarctic ice sheet, a warmer to colder stratosphere, and lesser to greater circumpolar sea ice extent. The year was also marked by several records, including the highest air temperature ever recorded on the continent (18.3°C, Francelino et al. 2021) that was observed on the northeastern tip of the Antarctic Peninsula on 6 February 2020. This temperature record was accompanied by the largest late-summer surface melt event yet recorded in the satellite data (since 1978) that affected more than 50% of the Antarctic Peninsula and reached elevations exceeding 1700 m. As described in Sidebar 6.1, the record warming and melting were caused by an exceptional atmospheric circulation pattern (an “atmospheric river”) that delivered extreme warmth and moisture from sub-tropical and middle latitudes to the West Antarctic region.

Later in the year, another record was broken with the longest-lived (and 12th-largest) ozone hole yet observed over the last 41 years. Below-average stratospheric temperatures were observed in winter and persisted well into spring 2020. These low austral spring temperatures stood in stark contrast to the year before when a dramatic stratospheric warming event occurred in September 2019. Both of these events had lasting effects on the climate: the 2020 event led to unusually high levels of ultraviolet radiation in the spring and summer of 2020/21 (section 6h), while the 2019 stratospheric warming event led to strong surface warming in spring and summer of 2019/20, particularly across Queen Maud Land (Clem et al. 2020a; Newman et al. 2020).

The shift from negative to positive net daily sea ice extent (SIE) anomalies in early August 2020 was particularly noteworthy as it marked the end of a long run of daily negative SIE anomalies that had persisted since the austral spring of 2016. This shift coincided with a strengthening and expansion of the Amundsen Sea Low during the latter half of 2020 in response to an evolving La Niña in the tropical Pacific. As discussed in Sidebar 6.2, responses to such perturbations emanating from the tropics, when extreme, have the potential to be “disruption events” at high southern latitudes and are associated with large shifts in the Antarctic climate system.

In the Southern Ocean, the most prominent anomalies observed during 2020 were a significant shoaling, freshening, and warming of two Subantarctic Mode Water production areas in the southeast Pacific and Indian Oceans, significant because these are key areas for global ocean uptake of heat and carbon. Deeper down, however, 2020 marks the continued reversal (since ~2014) of freshening and warming of Antarctic Bottom Water that had been previously observed over the last half century. On the continent, negative ice sheet mass anomalies, particularly on the Antarctic Peninsula and the Amundsen sector of the West Antarctic ice sheet, outweighed the small positive gains elsewhere.

More details on Antarctica’s climate, weather, ice, ocean, and ozone are presented below for 2020. In most sections, and as for previous years, the 2020 anomalies are derived through comparison with the 1981–2010 climatology if sufficient data are available (and when not, other date ranges are given). Place names mentioned throughout the chapter are provided in Fig. 6.1.

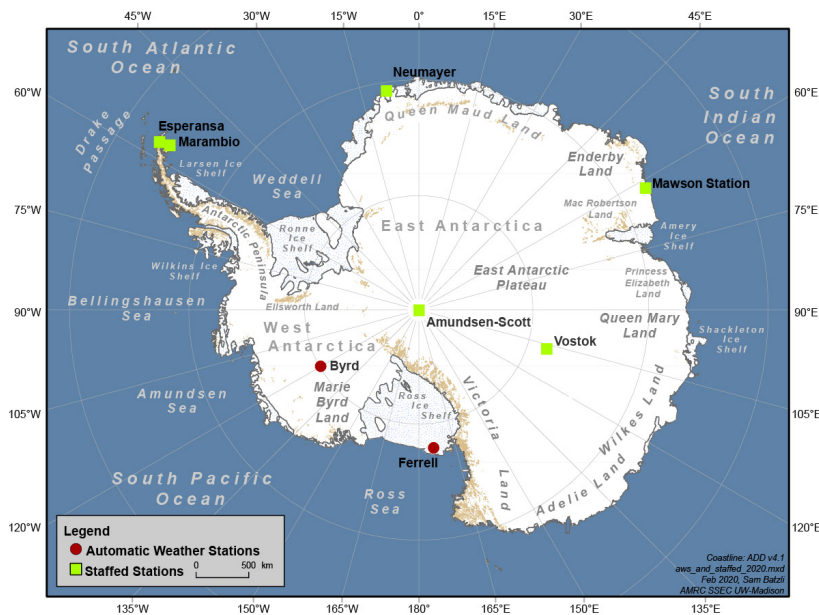


Fig. 6.1. Map of stations and other regions discussed in this chapter.

b. Atmospheric circulation and surface observations—K. R. Clem, S. Barreira, R. L. Fogt, S. Colwell, L. M. Keller, M. A. Lazzara, and D. Mikolajczyk

The 2020 Antarctic atmospheric circulation exhibited anomalous seasonal variability with large temperature swings on the continent and in the Weddell and Ross Sea sectors in particular. Meanwhile, East Antarctica experienced persistently warm conditions throughout much of the year. In the lower stratosphere and down through the troposphere, the year began with anomalously warm conditions associated with the late 2019 stratospheric warming event (Newman et al. 2020), while in contrast, 2020 finished with anomalously cold conditions in the stratosphere tied to an unusually large and deep ozone hole that developed during spring (see section 6h for more details).

The Antarctic atmospheric circulation anomalies were examined using the European Centre for Medium-Range Weather Forecasts fifth-generation atmospheric reanalysis (ERA5). Figure 6.2 shows the monthly geopotential height (Fig. 6.2a) and temperature (Fig. 6.2b) anomalies averaged over the polar cap (60°–90°S) and the monthly circumpolar zonal wind anomalies (Fig. 6.2c) averaged over 50°–70°S. The anomalies (contoured) and standard deviations (shaded) are relative to the 1981–2010 climatology. To summarize the surface climate anomalies, the year was split into four groups based on periods of relatively persistent surface pressure and temperature anomaly patterns: January–March, April–June, July–October, and November–December. The surface pressure and temperature anomalies (contours) and standard deviations (shaded) are averaged for each group relative to their 1981–2010 climatology (Fig. 6.3). Monthly temperature and pressure anomaly time series are also shown for select Antarctic staffed (Marambio, Neumayer, Mawson, Vostok) and automated (Ferrell AWS, Byrd AWS) weather stations (Fig. 6.4).

From January to March, geopotential height near the surface (Fig. 6.2a) and surface pressure (Fig. 6.3a) steadily decreased across the Antarctic continent while the midlatitudes were dominated by positive pressure anomalies. By March, tropospheric geopotential heights over the polar cap were more than 25 m (–1.5 std. dev.) below average, and surface pressure at all six weather stations ranged from –3 to –12 hPa below average. Concurrently, stronger-than-average circumpolar westerlies, peaking around $+2 \text{ m s}^{-1}$ (+1.5 std. dev.), developed through the troposphere and stratosphere, and the Southern Annular Mode (SAM) index reached its highest value of the year (+2.05) during March (Fig. 6.2c). Locally deep pressure anomalies were centered over Marie Byrd Land, the Ross Ice Shelf, and Wilkes Land (Fig. 6.3a, noting this shows a 3-month average). These cyclonic anomalies (particularly in February) produced warm northerly flow and positive surface air temperature anomalies of $+1^\circ$ to $+2^\circ\text{C}$ (+2 std. dev.) across the Antarctic Peninsula and Ross Ice Shelf during January–March, resulting

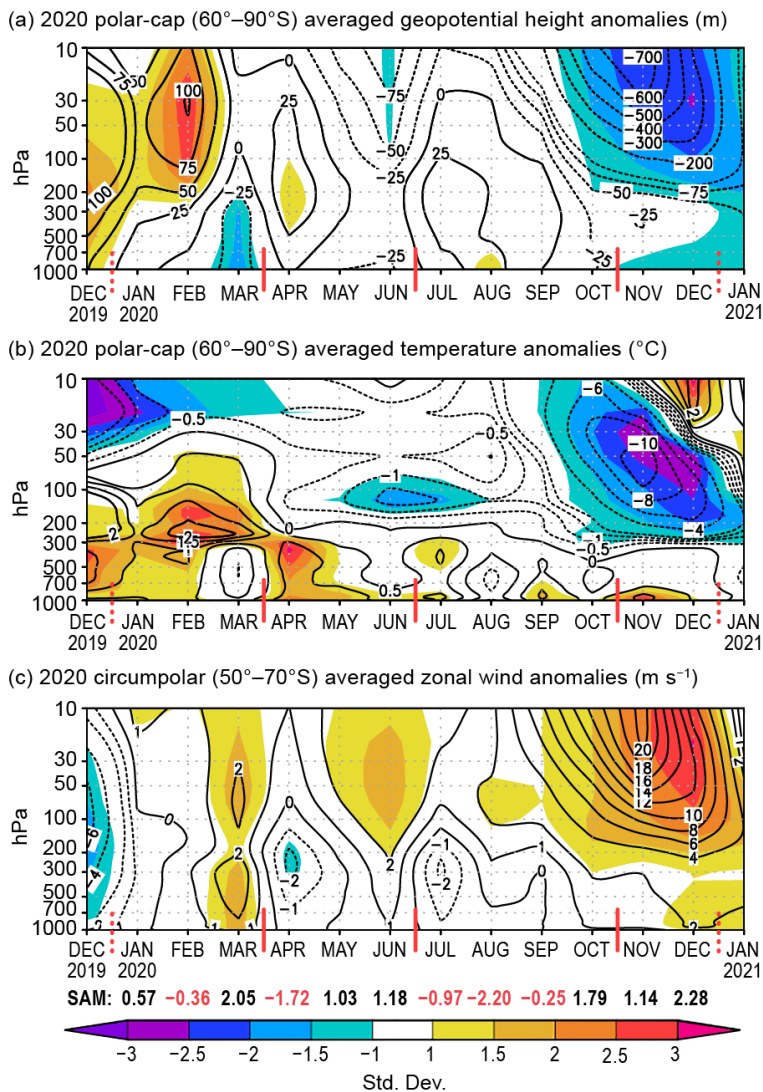


Fig. 6.2. Area-averaged (weighted by cosine of latitude) monthly anomalies over the southern polar region in 2020 relative to 1981–2010: (a) polar cap (60°–90°S) averaged geopotential height anomalies (contour interval is 25 m up to ± 100 m and 100 m after ± 100 m); (b) polar cap averaged temperature anomalies (contour interval is 0.5°C up to ± 2 °C and 2°C after ± 2 °C); (c) circumpolar (50°–70°S) averaged zonal wind anomalies (contour interval is 2 m s⁻¹ with an additional contour at ± 1 m s⁻¹). Shading depicts std. dev. of monthly anomalies from the 1981–2010 climatological average as indicated by color bar at bottom. Red vertical bars indicate the four climate periods used for compositing in Fig. 6.3; the dashed lines near Dec 2019 and Dec 2020 indicate circulation anomalies wrapping around the calendar year. Values from the Marshall (2003) SAM index are shown below (c) in black (positive values) and red (negative values). (Source: ERA5 reanalysis.)

in a new record high monthly mean temperature at Ferrell AWS of -10.7°C ($+3.8^{\circ}\text{C}$ above average) in February (Fig. 6.4e). Esperanza Station, on the northeastern side of the Antarctic Peninsula, recorded a temperature of $+18.3^{\circ}\text{C}$ on 6 February, the highest temperature recorded to date on the Antarctic continent replace with (Francelino et al. 2021). The causes of this record warming of the Antarctic Peninsula region are detailed in Sidebar 6.1.

Negative surface pressure anomalies of -4 to -6 hPa (-1 to -2 std. dev.) persisted across the Ross Ice Shelf and Marie Byrd Land from April through June (Figs. 6.3b, 6.4e,f), allowing anomalously warm conditions ($+2^{\circ}$ to $+3^{\circ}\text{C}$) to continue across the Antarctic Peninsula and adjacent Ellsworth Land through early winter. The warming also spread inland across the plateau during April–June (Figs. 6.3f, 6.4d) and polar cap averaged temperature anomalies were $+0.5^{\circ}$ to $+1^{\circ}\text{C}$ ($+1.5$ to $+2.5$ std. dev.) from April to June (Fig. 6.2b).

During July–October, the persistent low-pressure anomaly over the Ross Ice Shelf shifted northward into the Ross Sea (Fig. 6.3c). The broader surface pressure anomaly composite during this period (Fig. 6.3c) was consistent with a developing La Niña/Pacific–South American pattern (Yuan 2004), with high pressure east of New Zealand, low pressure over the Ross Sea, and high pressure in the Weddell Sea. Associated with this pattern in the South Atlantic region, Neumayer Station set a new record high monthly mean pressure of 995.7 hPa ($+10.9$ hPa above average) in August (Fig. 6.4b). The high-pressure anomaly in the Weddell Sea produced strong negative surface temperature anomalies of -7° to -9°C (>-3 std. dev.) across the Ronne Ice Shelf and the adjacent Filchner Ice Shelf to the east (Fig. 6.3g) from July through October, extending eastward along the coast to Neumayer Station, where a monthly temperature anomaly of -8.2°C was observed during August, coinciding with its record high pressure (Fig. 6.4b). The high-pressure anomaly in the Weddell Sea also ended the warm conditions on the Peninsula, and Marambio Station recorded its coldest August on record (-21.8°C , -8.7°C below average; Fig. 6.4a).

In contrast to the large fluctuations in the South Atlantic sector of Antarctica, surface pressures were near average to slightly above average over the remainder of the continent from April

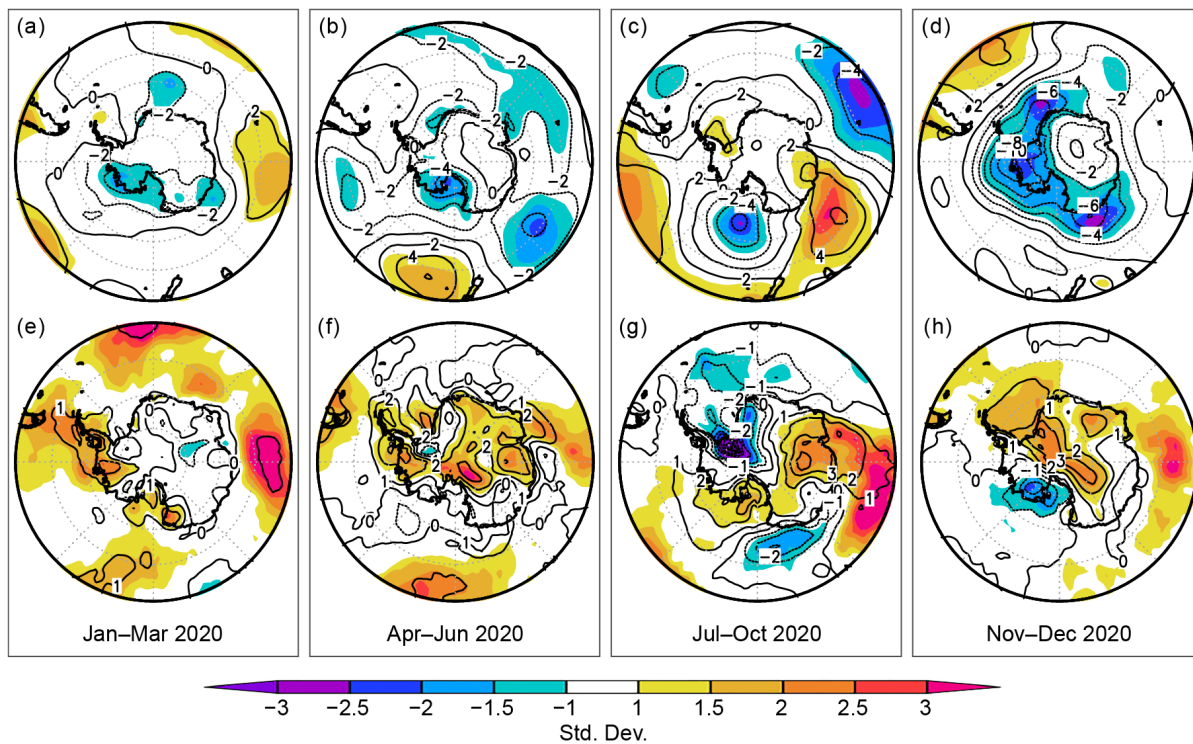


Fig. 6.3. (top) Surface pressure and (bottom) 2-m temperature anomalies relative to 1981–2010 for (a),(e) Jan–Mar 2020; (b),(f) Apr–Jun 2020; (c),(g) Jul–Oct 2020; (d),(h) Nov–Dec 2020. Contour interval is 2 hPa for surface pressure anomalies and 1°C for 2-m temperature anomalies. Shading depicts standard deviation of anomalies. (Source: ERA5 reanalysis.)

through October, extending upward through the troposphere (Figs. 6.2a, 6.3b,c, 6.4). In addition, a strong positive pressure anomaly developed just offshore of East Antarctica from 90° to 135°E during July–October (Fig. 6.3c), which produced positive surface temperature anomalies of +2° to +4°C (+2 std. dev.) across the Amery Ice Shelf and portions of the plateau (Fig. 6.3g). While no monthly record high temperatures were set here during this period, Mawson and Vostok stations observed persistently above-average temperature anomalies of +2° to +6°C from April to October (Figs. 6.4c,d), and Vostok Station experienced its warmest spring (September–November) on record (not shown).

The surface circulation underwent a dramatic shift during November and December, losing its La Niña-like wave train characteristics (Fig. 6.3d) and transitioning to a more zonally symmetric positive SAM pattern with below-average pressure over much of the continent and a deepened Amundsen Sea Low (Sidebar 6.2). However, the surface expression was not typical of most concurrent La Niña and positive SAM phases (Fogt et al. 2011). The strongest negative pressure anomalies were located over and near West Antarctica, where Byrd AWS recorded its lowest monthly pressure on record for October, November, and December (Fig. 6.4f), and Ferrell AWS (Fig. 6.4e) recorded its lowest pressure on record for December (both around –10 to –12 hPa). Concurrently, pressures over much of East Antarctica were near average. The regional low pressure over West Antarctica combined with relatively high pressures over East Antarctica produced anomalously warm conditions across the Weddell Sea and throughout much of the interior (Fig. 6.3h), where surface air temperatures were generally +2° to +3°C (+2 std. dev.) above normal; both Marambio (+3.8°C) and Vostok (+4°C) recorded their warmest Novembers on record (Figs. 6.4a,d). Below-average temperatures were found only across Marie Byrd Land and the Ross Ice Shelf during November and December, where southerly flow developed on the western side of the low pressure, marking a switch from the above-average temperatures that previously persisted here for much of the year.

In the stratosphere, strong negative geopotential height and temperature anomalies developed in October (Figs. 6.2a,b), associated with the anomalously large and deep ozone hole (section 6h). The geopotential height and temperature anomalies peaked in November at –700 m (–2 std. dev.)

and -10°C (-2.5 std. dev.), respectively. These anomalies strengthened the north–south pressure gradient and resulted in a strengthened stratospheric polar vortex of around 20 m s^{-1} in November (Fig. 6.2c). These strong anomalies in geopotential height, temperature, and winds persisted in the stratosphere through December, while much weaker anomalies characterized the troposphere. Whether the atypical regional nature of the surface circulation anomalies contributed to the unusually persistent ozone hole (section 6h), perhaps through a lack of planetary scale waves propagating from the troposphere to the stratosphere, remains an open question.

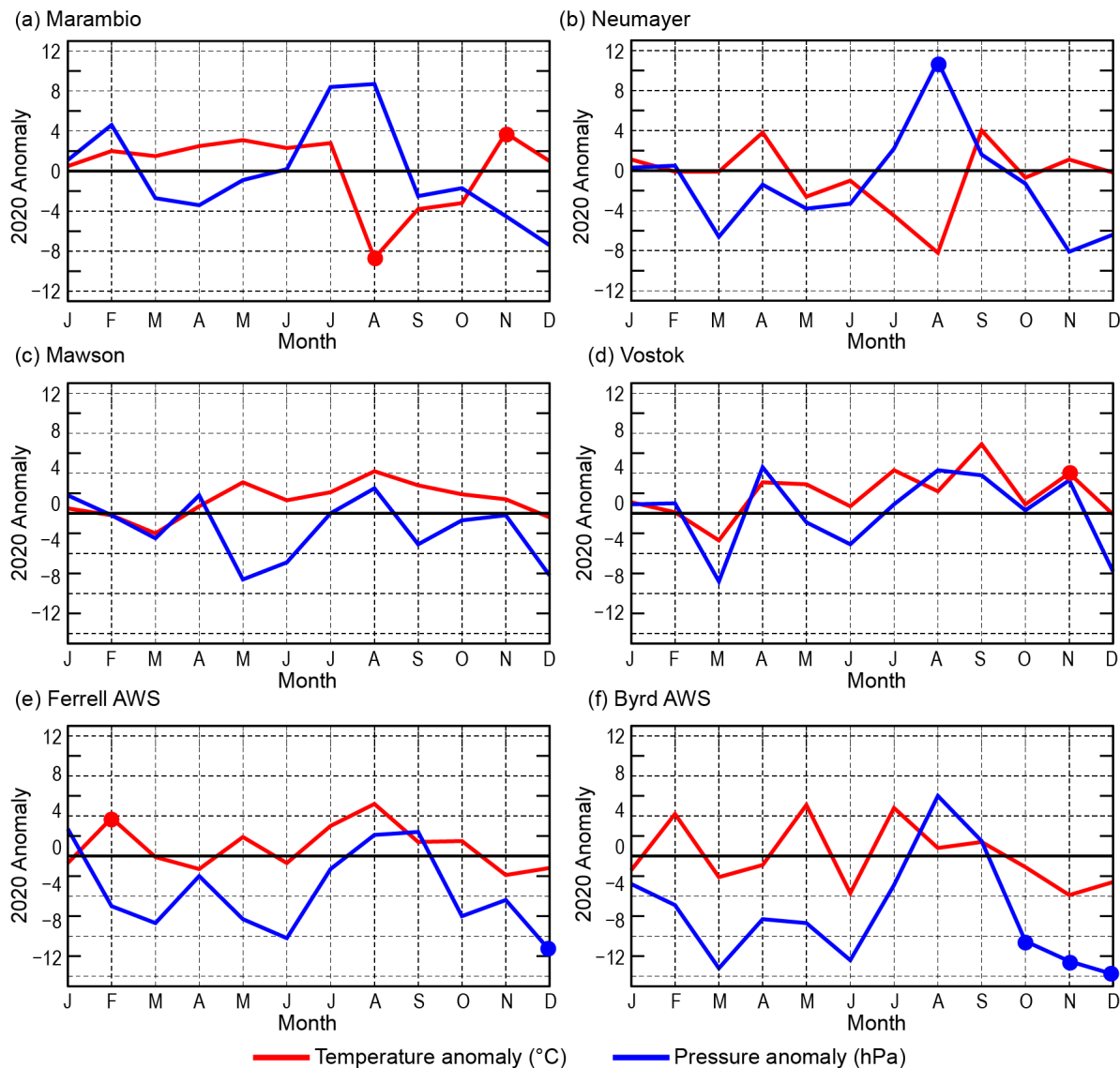


Fig. 6.4. Monthly Antarctic climate anomalies during 2020 at six representative stations [four staffed (a)–(d), and two automatic (e),(f)]. Anomalies for temperature ($^{\circ}\text{C}$) are shown in red and MSLP/surface pressure (hPa) are shown in blue, with filled circles denoting monthly mean records set for each station in 2020. All anomalies are based on differences from the monthly 1981–2010 averages. Observational data used to calculate records start in 1970 for Marambio, 1981 for Neumayer and Ferrell AWS, 1954 for Mawson, 1958 for Vostok, and 1980 for Byrd AWS.

Sidebar 6.1: Record warmth and surface melt on the Antarctic Peninsula in February 2020—K. R. CLEM, M. MACFERRIN, D. KENNETT, D. BOZKURT, AND T. SCAMBOS

On 6 February 2020, the Argentine research base, Esperanza, located on the northeast tip of the Antarctic Peninsula (AP; 63.4°S, 57.0°W, elevation 13 m a.s.l.), measured a 2-m temperature of 18.3°C (Francelino et al. 2021), which is the highest temperature ever recorded on the Antarctic continent, surpassing the previous record of 17.5°C (also at Esperanza) set on 24 March 2015. The AP also experienced its largest early-February surface melt extent on record, affecting more than 50% of the region and reaching elevations exceeding 1700 m a.s.l. on the Peninsula's southwestern side. As detailed below, these record events were tied to an exceptional atmospheric circulation pattern that brought extreme heat and moisture from sub-tropical and middle latitudes to the entire West Antarctic region, with surface warming on the eastern Peninsula being further intensified by the Foehn wind effect.

Figure SB6.1a shows the three-hourly surface synoptic conditions observed at Esperanza over the 5–7 February period (obtained from the Global Telecommunications System). Eighteen hours prior to the record, temperatures were steady around 0°C with high relative humidity between 80% and 90% and light and variable winds. Temperatures began increasing steadily between 0600 and 1200 UTC on 6 February and then increased rapidly during the 1200–1500 UTC period from 6.3°C (1200 UTC) to 18.3°C (1500 UTC). Coinciding with the sharp rise in temperature, relative humidity dropped to 27% and winds increased in speed while shifting from the northeast to the southwest. The synoptic conditions indicate the sudden rise in temperature was due to Foehn-related warming, which is common on the eastern Peninsula and characterized by a spike in temperature, a drop in relative humidity, and persistent westerly winds (Cape et al. 2015). Temperatures remained warm following the main spike with winds remaining strong out of the southwest, including 15.7°C observed 3 hours later (1800 UTC) and 17.3°C observed 6 hours later (2100 UTC), indicating a relatively long-duration Foehn event.

Foehn events are typically associated with high levels of moisture convergence on an upstream windward slope, which aids the rapid saturation of air as it ascends the slope (the western Peninsula). This causes the air to cool more slowly at about $-5^{\circ}\text{C } 1000 \text{ m}^{-1}$ (the saturated adiabat) than if it were not saturated. With less cooling, air crossing the ridge is far warmer than usual, allowing higher temperatures to be reached as the air descends the leeward slope (the eastern Peninsula) where it warms at about $+10^{\circ}\text{C } 1000 \text{ m}^{-1}$ (the dry adiabat). Indeed, the remarkable increase in temperature at Esperanza occurred shortly after landfall of an “atmospheric river” (AR;

outlined in green in Fig. SB6.1b) on the western Peninsula, which occurred at 0600 UTC on 6 February, 9 hours prior to the record temperature. Atmospheric rivers are long, narrow corridors of extremely high moisture flux (>85th percentile; Guan and Waliser 2015). Landfalling ARs in West Antarctica are unusual, with only around 12 events per year, but they are responsible for 40%–80% of surface melting in the region (Wille et al. 2019). The 6 February AR developed between a broad, double-barrel, low-pressure complex over the South Pacific (contours in Fig. SB6.1b), with a 960-hPa low in the western Amundsen Sea and a second 976-hPa low to its northeast near 50°S, and an area of strong (1024 hPa) high pressure centered over southern South America. Together, these features rapidly transported unusually warm, moist air sourced from 35°–40°S latitude poleward and eastward toward the AP, steered along the southern edge of the South America high-pressure cell.

The circulation pattern responsible for the 6 February AR was also remarkable. Figure SB6.1c shows averaged anomalies for the 4–10 February 2020 period of mean sea level pressure (MSLP, contours), surface air temperature (SAT, color), and surface wind (vectors) relative to the 1981–2010 4–10 February climatology. Along the northwest Peninsula and over Drake Passage, MSLP was more than 15 hPa (+2.5 std. dev.) above average. The exceptional nature of this high-pressure anomaly was even more apparent through the middle troposphere, where 4–10 February geopotential height along the northwest Peninsula from the 850-hPa to 500-hPa level was the highest on record (since 1979), including a 500-hPa geopotential height of 5505 m that was 296 m (+4 std. dev.) above average, shattering the previous record of 5357 m (148 m above average) set in 1998. Meanwhile, the low-pressure center in the Amundsen Sea was more than 12 hPa below average and the low pressure northeast of this region near 50°S was more than 6 hPa below average.

These strong circulation anomalies also advected extremely warm air into the region, producing positive SAT anomalies of more than 6°C across nearly all of West Antarctica and the AP. These anomalously warm temperatures, further enhanced by Foehn effect warming on the eastern Peninsula, caused anomalously large surface melt extents across the AP during a 7-day span from 6 to 12 February (Fig. SB6.1d). While the median melt extent from 1989 to 2020 is just 1%–2% for those dates, on 8 February 2020, surface melt reached 49.4% of the AP, breaking the previous satellite-measured record of 31.0% set on 8 February 1996. The next day on 9 February, surface melt reached 53.8% of the Peninsula, also a daily record, and

remained at record high levels (for the satellite record) through 12 February.

Similar circulation anomalies were seen during the previous record high Antarctic temperature on 24 March 2015 at Esperanza (Rondanelli et al. 2019), which also accompanied an AR that made landfall on the western Peninsula. Therefore, the anomalous circulation pattern described here appears exceptionally favorable for the development of ARs and is a key driver of extreme warmth and surface melt on the AP.

Previously it was shown that the 24 March 2015 circulation anomalies were forced by tropical convection (Rondanelli et al. 2019), with 6 February 2020 also exhibiting a pattern forced by tropical convection in the South Pacific Convergence Zone (Clem et al. 2019). Projections of future climate and surface melt extremes on the Peninsula will need to account for the occurrence and tropical linkages of this atmospheric circulation pattern, including a climate-driven tendency for increased Foehn frequency and intensity (Cape et al. 2015).

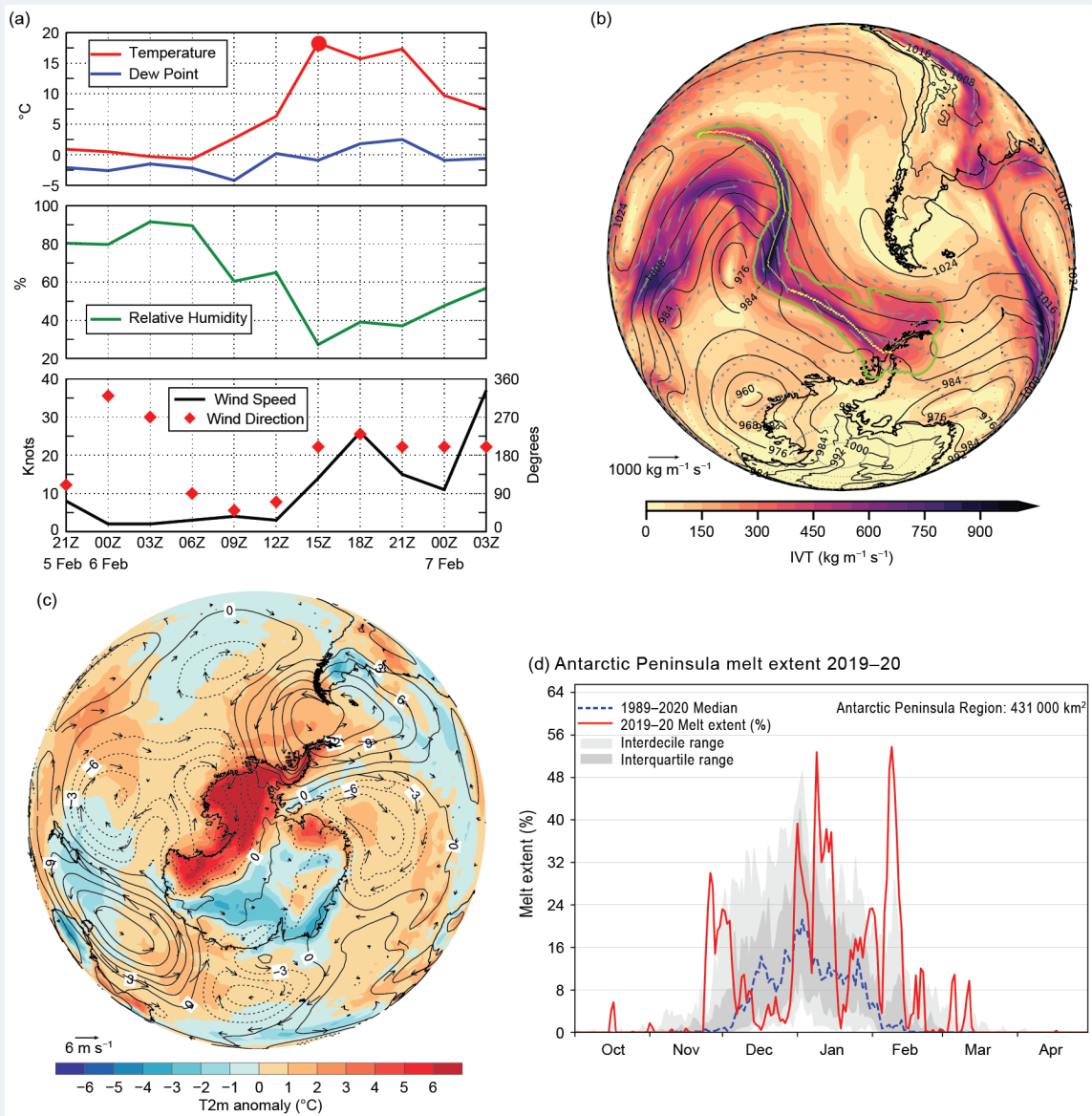


Fig. SB6.1. (a) Observed Esperanza synoptic conditions during 5–7 Feb 2020: (top) 2-m temperature and dew point ($^{\circ}\text{C}$, the red filled circle denotes the 18.3°C temperature record), (middle) 2-m relative humidity (%), and (bottom) 10-m wind speed (kt) and direction. (b) The atmospheric river (AR) that made landfall on the Antarctic Peninsula (AP) on 6 Feb 2020 at 0600 UTC: ERA5 integrated water vapor transport (IVT, $\text{kg m}^{-1} \text{s}^{-1}$; shaded/vectors), outline of AR/IVT exceeding 85th percentile for Jan–Mar 2020 (green contour) and ERA5 MSLP (hPa, black contours). The AR axis (yellow) denotes the pathway of maximum water vapor flux. (c) 4–10 February 2020 ERA5 MSLP (hPa, contour), 2-m temperature ($^{\circ}\text{C}$, shaded), and 10-m wind (m s^{-1} , vectors) anomalies relative to 1981–2010. (d) Daily totals of melt extent (%) over the AP (red line) from 1 Oct 2019 to 30 Apr 2020 from passive-microwave measurements (Meier et al. 2019). Daily median (dashed blue line), inter-quartile (dark gray shading), and inter-decile (light gray shading) ranges are included for the baseline period of Oct 1989 through Apr 2020.

c. Ice sheet surface mass balance—J. Lenaerts, E. Keenan, M. Maclennan, and T. Gorte

The grounded portion of the Antarctic ice sheet (AIS) is characterized by a frigid continental climate. Even in peak summer, atmospheric temperatures on the continent are low enough to prevent widespread surface melt (section 6d) or liquid precipitation, unlike the Greenland ice sheet (see section 5e). With few exceptions (e.g., the northern Antarctic Peninsula [AP]), any meltwater that is produced refreezes locally in the firm (compacted snow older than 1 year), making meltwater runoff negligible on the AIS. On the other hand, sublimation is a significant component of AIS surface mass balance (SMB; Lenaerts and Van Den Broeke 2012; Agosta et al. 2019; Mottram et al. 2021), especially in summer and on the flanks of the ice sheet where dry downsloping winds and blowing snow occur frequently (blowing snow >50% of the time; Palm et al. 2018). By far, the dominant contributor to AIS SMB, with a magnitude of about +2300 Gt (Gt = Gigatons = 10^{12} kg) yr^{-1} over grounded ice areas, is solid precipitation, i.e., snowfall.

Atmospheric reanalysis products are important tools for analyzing in near-real time AIS SMB and its two dominant components, snowfall and sublimation. Here we use reanalysis data from MERRA-2 at $0.5^\circ \times 0.625^\circ$ horizontal resolution (Gelaro et al. 2017) and ERA-5 at 0.28° horizontal resolution (Copernicus Climate Change Service [C3S] 2017) to analyze the 2020 AIS SMB, its spatial and seasonal characteristics, and its comparison to the climatological base period (1981–2010). Based on recent work comparing reanalysis products with in situ observations on Antarctica, MERRA-2 and ERA-5 were the best performing (Wang et al. 2016; Gossart et al. 2019; Medley and Thomas 2019); however, important biases remain that are associated with the relatively low spatial resolution of the reanalysis products and poor or no representation of important SMB

processes (e.g., blowing snow, clear-sky precipitation).

A time series of AIS SMB from 1980 to 2020 is provided, based on these two reanalysis products (Fig. 6.5a). The climatological (1981–2010) mean SMB is 2157 ± 131 Gt yr^{-1} in MERRA-2 and 2070 ± 113 Gt yr^{-1} in ERA-5. While both time series show comparable interannual variations, with year-to-year SMB differences of >300 Gt yr^{-1} between dry and wet years, neither of the reanalyses indicates a significant long-term trend in SMB. Furthermore, there is no significant trend in the difference between MERRA-2 and ERA-5 over the entire 1980–2020 period ($p = 0.58$), although there are periods when the two estimates agree more closely.

The 2020 SMB total and SMB anomaly were 2290 Gt and 133 Gt, respectively, for MERRA-2, falling outside the 1 standard deviation range in total SMB. Although 2020 AIS SMB was significantly higher than the 1981–2010 mean, 5 of the previous 40 years had a higher SMB, suggesting that 2020 was still within historical variability. As both reanalysis datasets produce similar results, we use MERRA-2 hereafter to focus on spatial and seasonal

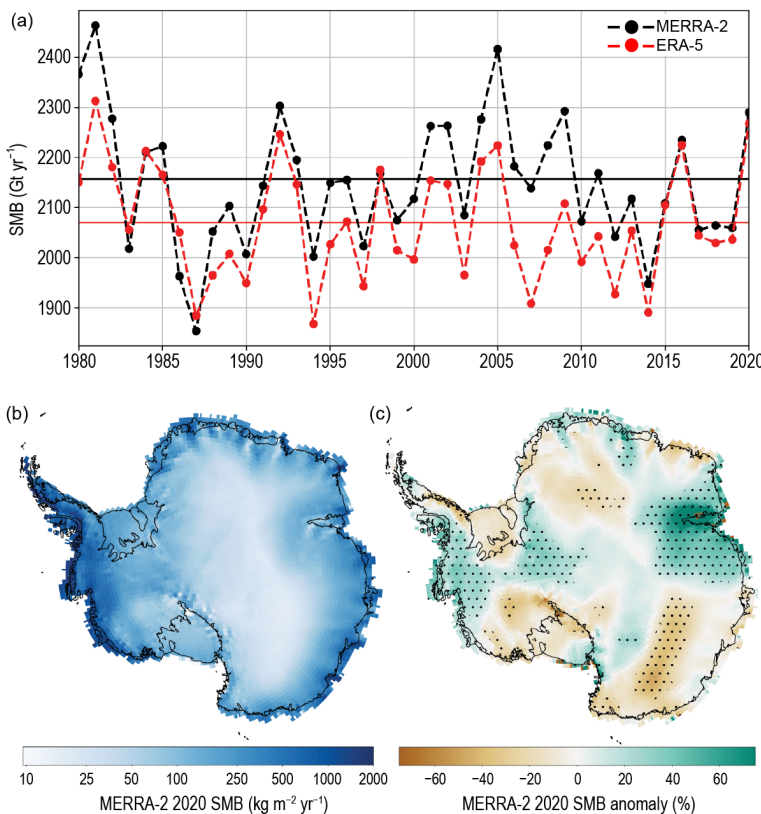


Fig. 6.5. Antarctic surface mass balance (SMB) in 2020. (a) Time series of annual Antarctic ice sheet integrated surface mass balance (Gt yr^{-1}) from 1980 to 2020, according to MERRA-2 (black) and ERA-5 (red) for the grounded portion of the ice sheet; horizontal lines are 1981–2010 means respectively. (b) and (c) 2020 SMB and SMB ($\text{kg m}^{-2} \text{yr}^{-1}$) anomaly(%) relative to 1981–2010 according to MERRA-2. In (c), 2020 SMB anomaly is higher than the 1981–2010 std. dev. in the stippled areas.

characteristics of the 2020 SMB. As described in many past studies, annual coastal AIS SMB is relatively high, e.g., >500 mm water equivalent (w.e.) in the western AP and coastal West Antarctic ice sheet (WAIS), decreasing sharply inland and with elevation on the ice sheet, e.g., <50 mm w.e. in the East Antarctic ice sheet (EAIS) interior (Fig. 6.5b). The year 2020 was no exception.

Our MERRA-2 results indicate substantial spatial variability in the 2020 anomaly relative to the 1981–2010 mean (Fig. 6.5c). In particular, 2020 SMB was substantially higher than climatology (>25%) along the areas of WAIS bordering the eastern Amundsen and Bellingshausen Seas, as well as the Amery Ice Shelf region on the EAIS, thus helping to offset part of the ice dynamic-based mass loss that is ongoing in West Antarctica (section 6e; Adusumili et al. 2021). On the other hand, 2020 SMB was low compared with the climatology (<–15%) in western Queen Maud Land and Wilkes Land, marking a brief reversal of recent high-accumulation years there (Lenaerts et al. 2013). Additionally, 2020 SMB was significantly below average in Marie Byrd Land, which, along with the positive SMB anomaly farther east, is remarkably consistent with the observed long-term SMB trends in West Antarctica (Medley and Thomas 2019).

Seasonally, the climatological (1981–2010) AIS SMB varies considerably (Fig. 6.6), with a minimum in austral summer (less than 140 Gt month⁻¹) and maximum in austral autumn and winter (more than 200 Gt month⁻¹). For 2020, the first 3 months (January–March) and last 3 months (October–December) were well within the 1 standard deviation range (gray shading) relative to the 1981–2010 period. Comparing the 2020 anomaly with the long-term mean and standard deviation (Fig. 6.6, black line and gray shading) indicates that the high SMB values in April, May, and July, as well as the low SMB values in August, were statistically significant (>1 std. dev.). The drastic difference between the July and August total SMB values reflects anomalously high and low snowfall in those 2 months, respectively, in the West Antarctic region bordering the eastern Amundsen and Bellingshausen Seas. The high snowfall in July was associated with a juxtaposition of strong positive pressure anomalies over the AP and strong negative pressure anomalies over the eastern Ross Sea (see Fig. SB6.3a) that funneled warm moisture-laden air over the West Antarctic coastal region. The positive pressure anomaly shifted east of the AP in August, the atmospheric circulation became more zonal west of the AP (Fig. SB6.3b), and the delivery of warm moisture-laden air from the north sharply decreased to this area (see also section 6f and Sidebar 6.2 for the corresponding sea ice response).

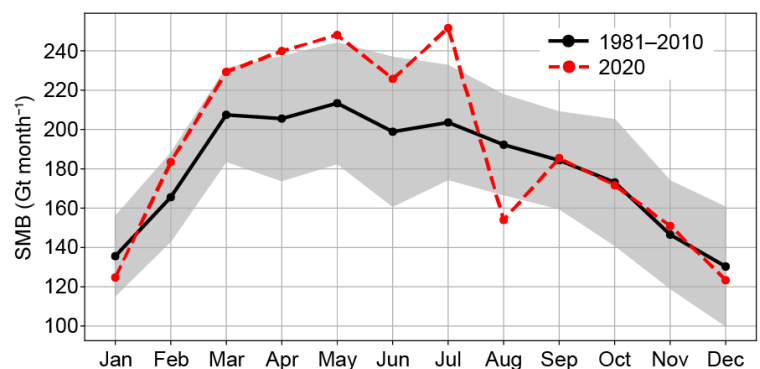


Fig. 6.6. Seasonal cycle of (grounded) AIS-integrated SMB according to MERRA-2 for 2020 (red) and 1981–2010 climatology (black line shows the mean, gray shading is ± 1 std. dev.).

d. Ice sheet seasonal melt extent and duration—M. MacFerrin, T. Mote, L. Wang, H. Liu, L. Montgomery, and T. Scambos

Surface melt on the Antarctic Ice Sheet (AIS) occurs primarily on the coastal margins, especially on the Antarctic Peninsula (AP) and Antarctic ice shelves. It is generally not a large component of Antarctica’s net surface mass balance because few areas have significant runoff of meltwater. However, surface melt has a major effect on the density of the underlying glacial firn (compacted snow older than 1 year) and can induce crevasse deepening, calving, or glacier acceleration through hydrofracture and input of water to the ice–bed interface. Because the austral melt season (defined here as 1 October through 30 April) spans two calendar years, we focus here on the 2019/20 melt season. (Next year’s report will discuss the 2020/21 melt season.) The season bounded by October

2019 through April 2020 had well-above-average melt anomalies in several regions when compared to their long-term average (here, 1989–2020). The AP had an especially strong melt season (Banwell et al. 2021).

Daily surface melt was mapped using satellite passive microwave brightness temperature data, obtained as daily-composited polar stereographic products from the National Snow and Ice Data Center (products NSIDC-0001 and NSIDC-0007; Meier et al. 2019; Gloerson 2006) spanning 1979–present. Daily passive microwave brightness temperatures using the 37 GHz horizontal polarization channel have been acquired by the SMMR, SSM/I, and SSMIS sensors aboard the NOAA Nimbus-7 and DMSP F8, F11, F13, F17, and F18 satellites. Surface melt was determined by brightness temperatures that exceeded a dynamically established threshold using a simple microwave emission model of the expected presence of liquid water in near-surface layers of ice and snowpack. The method used here was first developed to track Greenland’s ice sheet surface melting on a daily basis (Mote and Anderson 1995, 2007, 2014). However, large seasonal fluctuations in brightness temperature from areas of dry polar firn in Antarctica can create false positive melt in an unmodified version of the Greenland algorithm. False positives were identified by filtering cells that have a negative 18V minus 37V GHz frequency gradient (SMMR) or 19V minus 37V GHz frequency gradient (SSM/I), and were removed if the measured brightness temperature only marginally exceeded the modeled melt threshold (<10 Kelvin).

During the SMMR sensor period (1979–87), passive microwave composite data are only available every other day. To address the daily temporal gaps, melt extent totals are interpolated between days, or if longer temporal gaps are present, the gaps are filled with the long-term mean value. For error assessment however, the SSMI sensor period (1989–2020) is used as the baseline given the higher quality (i.e., not interpolated) SSMI-derived melt data (e.g., Figs. 6.7b, SB6.1d). An ice extent mask of 25-km grid cells for the AIS was developed from the Quantarctica v3.0 Detailed Basemap dataset (Norwegian Polar Institute 2018). All 25-km cells that contained $\geq 50\%$ land ice or ice shelf were included, while coastal cells that contained a large fraction of sea ice or open ocean were excluded. We divided the AIS into seven regions that comprise the main drainage basins (following Shepherd et al. 2012; Fig. 6.7).

Figure 6.7a shows the AIS melt extent and total number of melt days for the 2019/20 melt season. More than 60% of the total AIS surface melt occurred on the AP, which had large melt events in November, January, and February (Fig. SB6.1d). These large melt events were caused by warm atmospheric rivers from the southern Pacific Ocean and record high temperatures on the

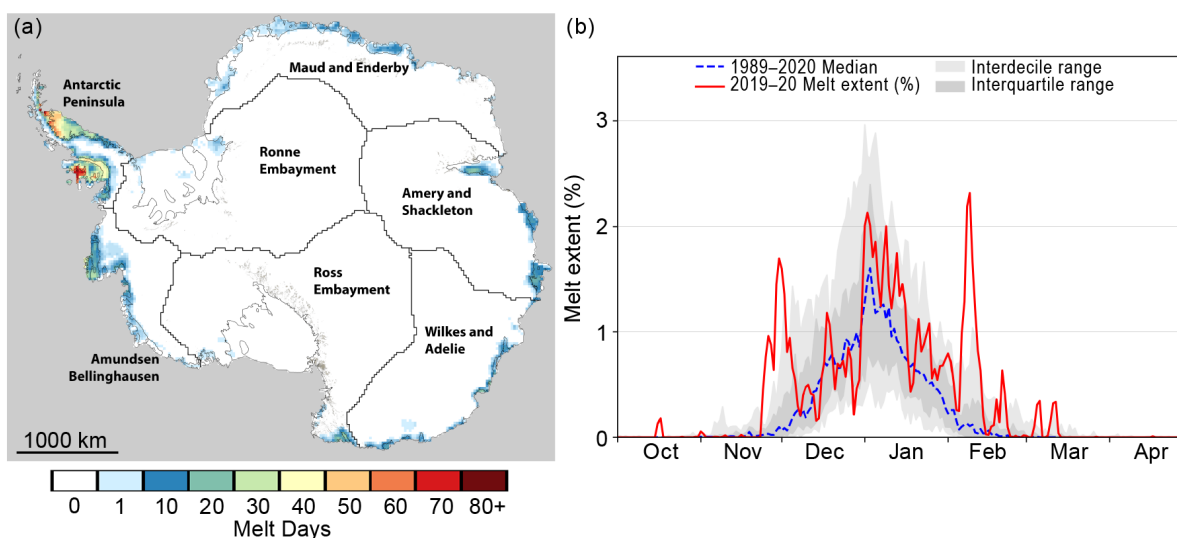


Fig. 6.7. Surface melt across the Antarctic ice sheet as detected from passive microwave satellites. (a) Map of the sum of melt days from 1 Oct 2019 to 30 Apr 2020, with Antarctic sub-regions outlined and labeled. (b) Time series of melt (%) for all of Antarctica (red) compared to median daily values (blue), inter-quartile ranges (dark gray), and inter-decile ranges (light gray) from the 1989–2020 base period.

Peninsula (Sidebar 6.1; Clem et al. 2019). The February 2020 melt event set a late-season record for the 1979–2020 period, for both the AP region (Fig. SB6.1d) and for the entire ice sheet (Fig. 6.7b). The Amery and Shackleton ice shelves, most of the coast of Wilkes Land in East Antarctica, and the Amundsen-Bellinghousen region in West Antarctica also saw above-average melt in 2019/20, although not as pronounced as the melt events on the Peninsula. Comparatively, the Ronne and Ross ice shelves experienced lower-than-average melt conditions.

Long-term trends in annual melt index (the sum of daily melt extent [$10^6 \text{ km}^2 \cdot \text{days}$] for each year; Zwally and Fiegles 1994; Liu et al. 2006) show general declines in surface melt during the 42-year satellite record for the AIS (Fig. 6.8a), dominated by the decline in melt on the AP (Fig. 6.8b).

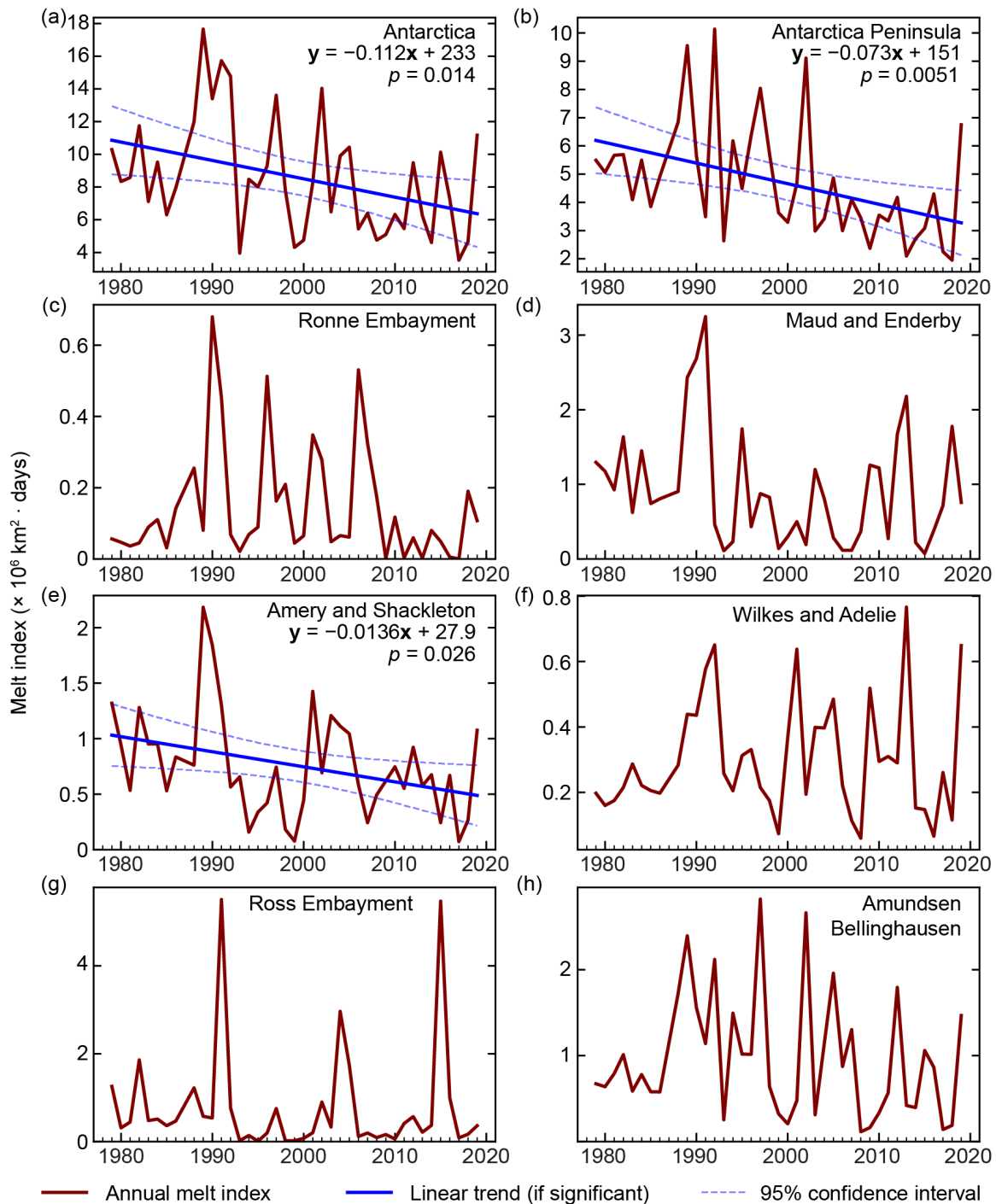


Fig. 6.8. Long-term time series of annual melt index ($\times 10^6 \text{ km}^2 \cdot \text{days}$) for the 1979–2020 satellite record for (a) all of Antarctica and (b)–(h) each sub-region labeled in Fig. 6.7a. Trend lines and 95% trend confidence intervals are outlined in blue where the p -values of the slopes are statistically significant ($p \leq 0.05$). Due to a 41-day gap in satellite observations from Dec 1987–Jan 1988, the 1987 melt season is omitted from these time series.

This negative trend is consistent with previous studies of satellite-observed melt since the late 1970s (Liu et al. 2006; Tedesco 2009; Barrand et al. 2013; Oliva et al. 2017), but contrasts with a warming of West Antarctica (including the Peninsula) since the mid-twentieth century that then leveled off at the start of the twenty-first century (Turner et al. 2016). A statistically significant reduction in surface melt was also observed for the Amery-Shackleton region of East Antarctica (Fig. 6.8e), but the trend accounts for only 12% of the continent-wide signal, as opposed to 65% from the AP. Other regions of the AIS show large interannual variability in surface melt but no statistically significant trends over the satellite record.

A recent study (Montgomery et al. 2020) reported on a newly identified firn aquifer in Antarctica located on the Wilkins Ice Shelf to the southwest of the AP (Fig. 6.1). Because firn aquifers are hydrological features in ice sheets or ice shelves that can store large amounts of surface meltwater in the subsurface firn, identifying firn aquifers is relevant for assessing the impacts of Antarctic surface melt. Firn aquifers form in areas of high melt and high snow accumulation, where large volumes of meltwater percolate several meters into firn pore spaces and where meltwater can be stored through winter without refreezing (Kuipers-Munneke et al. 2014). Previously, firn aquifers were only observed in mountain glaciers and in the Greenland ice sheet (Fountain and Walder 1998; Forster et al. 2014). The recent study by Montgomery et al. (2020) shows that the Wilkins Ice Shelf firn aquifer is highly permeable, based on assessments of borehole permeability at the level of the aquifer and on observed drawdown of the water table in a nearby rift. Previously, very rapid calving events were observed on the Wilkins Ice Shelf (Scambos et al. 2009) and were likely a result of hydrofracture, driven by the extensive aquifer (Montgomery et al. 2020). Another recent study using modeling shows favorable conditions for aquifers on other AP ice shelves, such as the remnants of the Wordie Ice Shelf (van Wessem et al. 2020), and indeed additional aquifers have been identified in the field near the Wilkins Ice Shelf (MacDonnell et al. 2021). Given the key role firn aquifers play in ice shelf and ice sheet stability and the ongoing efforts in mapping of their distributions, we will continue to report on aquifer research in the coming years.

e. Ice sheet changes from satellite observations—A. Gardner, S. Adusumilli, and H. A. Fricker

The Antarctic ice sheet (AIS) gains mass through accumulation (total snowfall minus melt runoff and sublimation; see section 6c) and loses mass primarily by processes occurring at the coasts: seaward ice flow and iceberg calving (which generally has an episodic, multidecadal cycle) and basal melt of floating ice (continuous, but time-varying with ocean heat flux; Depoorter et al. 2013). For any given time period, the net mass balance of the competing loss and gain terms depends on interactions between ice, ocean, and atmosphere. Averaged over long-time scales, ice loss from calving and basal melt are approximately equal (Rignot et al. 2013) and seasonal effects are minimized. If the AIS were in steady-state, their sum would offset the mass gain from net accumulation. In the *State of the Climate in 2019* report, we reviewed long-term changes in AIS mass over the period 1992–2019 and discussed the processes to which they are attributed (Fricker and Gardner 2020). Over that period, the AIS experienced a rapid increase in ice discharge to the ocean and inland dynamic thinning (elevation lowering), largely driven by increased rates of ice sheet thinning and grounding-line retreat concentrated along the Amundsen Sea coast.

A recent, and more precise, estimate of decadal change in AIS mass comes from Smith et al. (2020) and is based on high-accuracy laser altimetry data acquired by NASA's ICESat (2003–09) and ICESat-2 (2018–19). The Smith et al. study corroborated the scale and location of previously reported (e.g., Shepherd et al. 2018) ice sheet mass losses in West Antarctica that were partially offset by mass gains in parts of East Antarctica, with a net grounded ice mass loss of 118 Gt yr⁻¹, adding an estimated total of 5.5 mm to sea level over the 2003–19 period. ICESat-2 data can now be used to show changes on shorter timescales that reveal drivers of elevation changes over shorter intervals, such as accumulation events and/or firn compaction (i.e., compacted snow older than 1 year). For example, ICESat-2 data revealed increases in ice sheet surface elevation in West Antarctica between April 2019 and June 2020 (Adusumilli et al. 2021); 41% of these height

changes were due to extreme precipitation, and half of this precipitation occurred as a result of “atmospheric rivers,” strong frontal systems that transported large amounts of water (here, primarily as snow) from lower latitudes to the Antarctic continental interior (section 6c; Sidebar 6.1; Lenaerts et al. 2020).

For this report we derived estimates of ice sheet surface height from NASA’s ICESat-2 laser altimeter over the period November 2019 to November 2020, as well as mass anomalies over this same period from NASA’s satellite gravimeter (GRACE-FO; Wiese et al. 2019). Conversion of height differences to mass differences requires a firn density model (e.g., Ligtenberg et al. 2011) to establish the relationship between height and mass, but this model was not available for this report. The derived ice sheet surface height estimates are from the ATLAS/ICESat-2 L3A Land Ice Height, Version 3 data product (Smith et al. 2021; <https://nsidc.org/data/ATL06/versions/2>) that provides precise estimates of height along ground tracks. Height changes were determined by differencing two, 3-month averages centered on November 2019 and November 2020 (Fig. 6.9a), smoothed using a 30-km Gaussian filter. Surface mass anomalies were derived from JPL GRACE and GRACE-FO (Wiese et al. 2019; https://podaac.jpl.nasa.gov/dataset/TELLUS_GRAC-GRFO_MASCON_CRI_GRID_RL06_V2), which solve for mass anomalies from the satellite gravimeters and were determined on 300-km diameter spherical caps (Wiese et al. 2019). For the November 2019 to November 2020 period, the annual analysis included estimates derived from GRACE-FO data only, and the gravity-derived mass anomalies were calculated for the same period as the altimetry, using the same 3-month averaging. To determine ice sheet mass anomalies in units of ice equivalent height changes (Fig. 6.9b), we identified all grids (or mass concentration blocks, i.e., mascons) located within the provided land mask that contain more than 10,000 km² of land. We then interpolated area-averaged rates of change using natural neighbor interpolation according to the location of the land-weighted mascon centroid. We excluded all non-land areas inclusive of ice shelves, noting that GRACE is insensitive to changes in ice shelf mass.

Our maps (Fig. 6.9) show ongoing losses in West Antarctica, specifically in the Antarctic Peninsula and the Amundsen Sea sector, and in East Antarctica, specifically Enderby, Wilkes (Totten Glacier), and Oates Lands (Cook Glacier). Many of the increases in height around Antarctica correspond well with positive surface mass balance anomalies reported for 2020 (Fig. 6.5c), which suggests a major contribution of surface processes in driving sub-annual height and mass changes during this period. The exception was the Amundsen Sea sector, which experienced net mass loss due to grounded ice discharge and surface lowering outweighing the positive surface mass balance anomaly (Fig. 6.5c).

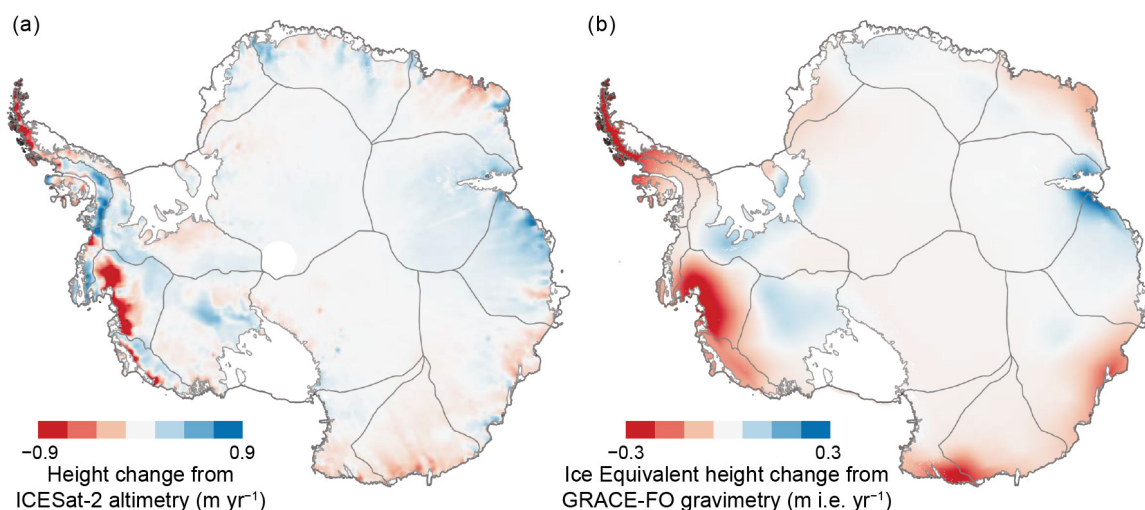


Fig. 6.9. (a) Height change (m yr⁻¹) from ICESat-2 and (b) ice equivalent (i.e.) height change (m i.e. yr⁻¹) from GRACE-FO for the period Nov 2019 to Nov 2020.

There were no major calving events from the large ice shelves in 2020, unlike 2019 with the calving of iceberg D-28 from the Amery Ice Shelf (Walker et al. 2021; Francis et al. 2021). However, the ice front of Pine Island Ice Shelf, a rapidly thinning ice shelf in the Amundsen Sea sector (Paolo et al. 2015), retreated to its most landward location observed in recent decades following a small calving event (~200 km²) in February 2020 (Lhermitte et al. 2020).

f. Sea ice extent, concentration, and seasonality—P. Reid, S. Stammerjohn, R. A. Massom, S. Barreira, T. Scambos, and J. L. Lieser

Antarctic sea ice plays a crucial role in the global climate system and is highly sensitive to climate change and variability (Walsh 1983; Liu et al. 2002; Roach et al. 2020). Sea ice seasonally covers a vast area of the high-latitude Southern Ocean each year, expanding its extent from ~3 × 10⁶ km² in summer to 19–20 × 10⁶ km² in winter (Parkinson 2019). This seasonal cycle is driven by large-scale atmospheric and oceanic circulations and temperature, but on shorter time scales is highly sensitive to the frequent occurrence of high wind and wave events, and also serves as a physical buffer for those ice shelves vulnerable to the destructive effects of ocean swells (Massom et al. 2018). As a highly reflective, insulative blanket, the sea ice and its snow cover strongly modify ocean–atmosphere fluxes and interactions (Bourassa et al. 2013). In turn, sea ice processes are of high importance to the physical and chemical properties and dynamics of the high-latitude ocean and atmosphere, including global ocean overturning (thermohaline) circulation (Meredith and Brandon 2017). The modification of ocean salinity and stratification by sea ice growth/melt processes moderates climate change by regulating the Southern Ocean’s capacity to take up and store anthropogenic heat and carbon from the atmosphere (Frölicher et al. 2015), while more locally these same sea ice processes modify warm ocean-water incursions to Antarctic outlet glaciers and ice shelves and thus basal melt rates (Timmermann and Hellmer 2013). Sea ice also forms a key habitat for a myriad of biota—ranging from micro-organisms to whales (Thomas 2017)—that are highly adapted to (and dependent on) its presence and seasonal changes (Massom and Stammerjohn 2010). Human activities around Antarctica such as the resupply of research stations and field experiments are also strongly affected by sea ice (COMNAP 2015). Given these factors, changes and variability in Antarctic sea ice have important ramifications.

Based on past assessments of the satellite passive microwave record, net Antarctic sea ice extent (SIE) had a small positive trend of 1.0% ± 0.5% per decade from 1979 to 2018 (Parkinson 2019) that consisted of contrasting regional and seasonal contributions (Stammerjohn and Maksym 2017). In the past decade, however, Antarctic sea ice coverage transitioned from persistently positive daily SIE anomalies and record highs during 2012 to mid-2015 (Reid and Massom 2015) to persistently negative daily SIE anomalies and record lows during late 2016 to early 2020 (Reid et al. 2020).

Now in 2020, after three and a half years of persistently negative net SIE anomalies, SIE rebounded close to the 1981–2010 average both in March and June and then remained above the long-term average from mid-August through mid-December (Fig. 6.10a). Annual minimum SIE in 2020 occurred on 19 February (2.71 × 10⁶ km², slightly below average), and the maximum on 25 September (19.06 × 10⁶ km², slightly above average). Sea surface temperatures to the north of the sea ice were generally above average earlier in the year, before transitioning to below or near average later in the year (e.g., Figs. 6.10c,d; see also section 6g, Fig. 6.12f). Large-scale atmospheric circulation patterns around Antarctica varied quite strongly during 2020 (section 6b, Fig. 6.3), greatly influencing the regional distribution of sea ice. Hence, the following description of the seasonal and regional evolution of sea ice closely follows the four climate periods described in section 6b.

Early 2020 was characterized by weakened westerly winds and a negative Southern Annular Mode (SAM) index value that was accompanied by a strengthening of westerly winds and positive SAM value in March (Fig. 6.2c). Westerly winds generally cause ice divergence away from the continent (Hall and Visbeck 2002), such that the strengthened westerly winds in early 2020 contributed to a rebound of summer SIE from persistently negative in January–February

to near-average in March, particularly in the western Weddell Sea (Fig. 6.10c). There was also a slightly stronger-than-normal Amundsen Sea Low (ASL) in early 2020 located at $\sim 170^\circ\text{W}$ (Fig. 6.3a) that contributed to decreased SIE in the eastern ($\sim 140^\circ\text{--}160^\circ\text{W}$) Ross Sea and slightly increased SIE in the western ($\sim 150^\circ\text{--}170^\circ\text{E}$) Ross Sea (Fig. 6.10b). The central Weddell Sea region ($\sim 20^\circ\text{--}40^\circ\text{W}$) also had much lower-than-normal SIE (Fig. 6.10b), a summer anomaly pattern that has persisted since 2017 (Turner et al. 2020).

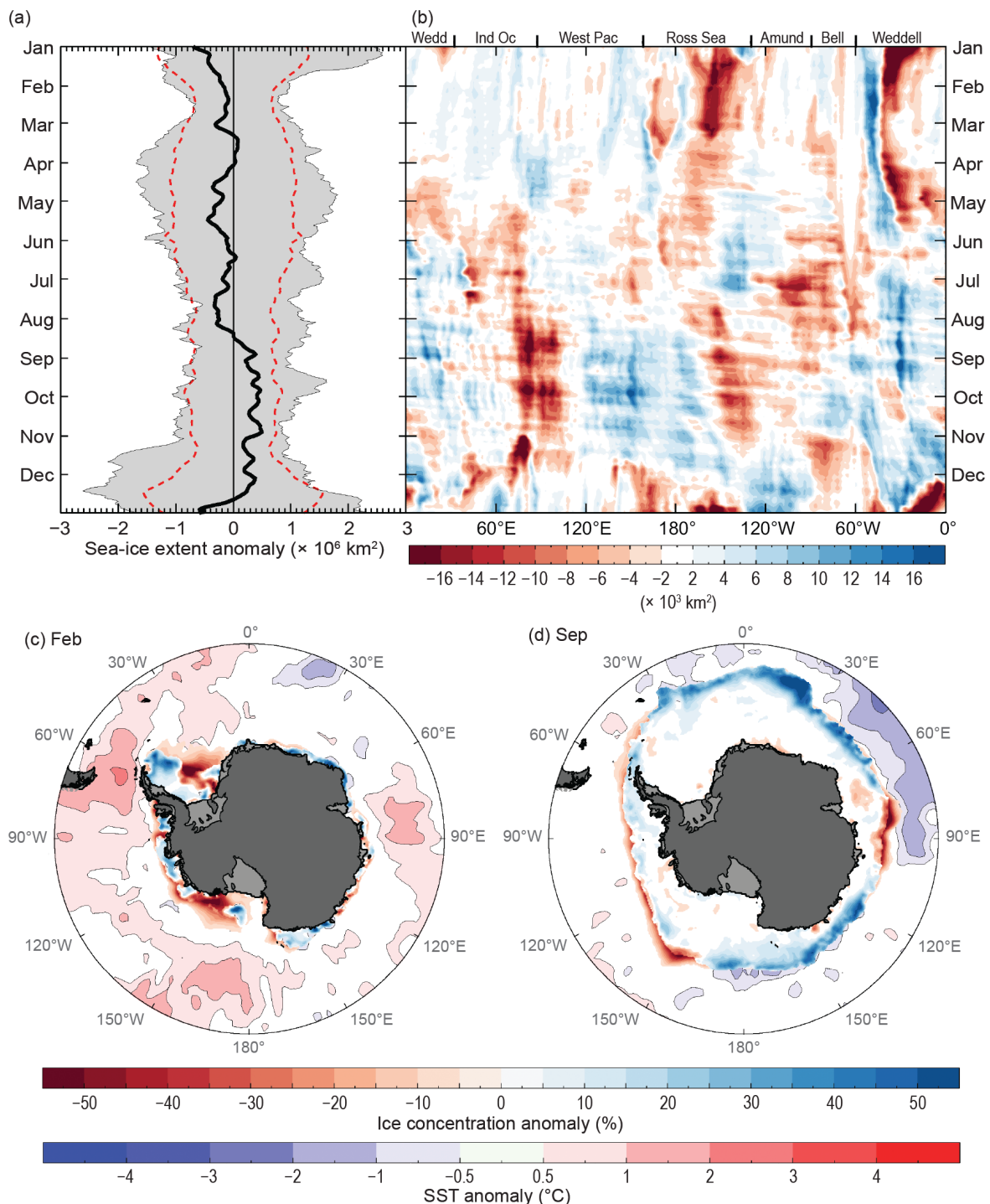


Fig. 6.10. (a) Time series of net daily sea ice extent (SIE) anomalies ($\times 10^6 \text{ km}^2$) for 2020 (solid black line) relative to 1981–2010. The gray shading represents historical (1979–2018) daily SIE anomalies; dotted red contours are the ± 1 std. dev. (b) Hovmöller (time–longitude) representation of daily SIE anomalies ($\times 10^3 \text{ km}^2$ per degree of longitude) for 2020. Maps of sea ice concentration anomalies (%) and sea surface temperature anomalies ($^\circ\text{C}$; Reynolds et al. 2002; Smith et al. 2008) for (c) Feb and (d) Sep 2020. Sea ice concentration is based on satellite passive microwave ice concentration data (Cavalieri et al. 1996, updated yearly, for climatology and Maslanik and Stroeve 1999, for the 2020 sea ice concentration). See Fig. 6.1 for relevant place names.

In April, circumpolar surface westerly winds weakened again (Fig. 6.2c), and the net SIE anomaly became more negative (Fig. 6.10a), followed by the development in May of a zonal wave-3 pattern in the longitudinal distribution of SIE (Fig. 6.10b). The zonal wave-3 pattern was caused by atmospheric low-pressure systems centered at $\sim 130^\circ\text{W}$, $\sim 70^\circ\text{E}$, and $\sim 140^\circ\text{E}$ that led to contrasting SIE anomalies to the east/west of these three low-pressure centers. The zonal wave-3 pattern also resulted in corresponding early/late regional anomalies in the timing of ice-edge advance (Fig. 6.11a).

The austral winter of 2020 was characterized by a transition to persistently positive net SIE anomalies starting in August in association with a developing (but relatively weak at the time) La Niña that initially resulted in a strengthened ASL at $\sim 160^\circ\text{W}$ that thereafter expanded toward $\sim 140^\circ\text{W}$ during September–November (Sidebar 6.2; Stammerjohn et al. 2008; Yuan 2004). The ASL in August also comprised a zonal wave-2 atmospheric pattern, with an additional negative pressure anomaly at $\sim 70^\circ\text{E}$, separated by a high-pressure ridge at $\sim 140^\circ\text{E}$ (Figs. 6.3e, SB6.3b). This zonal wave-2 pattern resulted in increased/decreased SIE in the Ross Sea/Amundsen-western Bellingshausen Seas (Figs. 6.10b,d), somewhat characteristic of La Niña periods (Sidebar 6.2). During September, SIE was also more extensive (positive anomaly) from the western Weddell Sea to the Indian Ocean sector ($\sim 30^\circ\text{W}$ to $\sim 70^\circ\text{E}$) and the eastern Pacific region through to the Ross Sea sector ($\sim 120^\circ\text{E}$ to $\sim 160^\circ\text{W}$), with reductions (negative SIE anomalies) elsewhere (Figs. 6.10b,d). From September through October, negative SIE anomalies were prevalent between $\sim 160^\circ\text{W}$ and 90°W , in conjunction with warm northerly winds along the eastern limb of the expansive low-pressure anomaly. Interestingly, there was late-season sea ice growth in the eastern Bellingshausen Sea region from $\sim 60^\circ$ to 80°W , i.e., just outside (eastward) of the low-pressure anomaly region, influenced by the ASL as described above.

From November through the end of the year, the ASL began to weaken, the circumpolar atmospheric trough deepened southward, and the SAM index became positive again. The enhanced circum-Antarctic cyclonic activity altered the regionality of sea ice coverage as the annual retreat season progressed. In most regions (except for the Amundsen Sea region) and during December, net SIE decreased sharply (Fig. 6.10a), particularly within the two major gyre embayments of the Ross and Weddell Seas (Figs. 6.10b, 6.11b), as often happens in late spring in response to the southward deepening of the circumpolar trough (e.g., Watkins and Simmonds 1999). Seasonally, the net result was a longer ice season in most of the outer pack (except for the Bellingshausen Sea and eastern Indian Ocean areas), contrasted against a shorter ice season in the inner pack (Fig. 6.11c). In further contrast, the ice season in the Bellingshausen Sea in 2020 was anomalously short but in-line with the long-term trend in that region (Fig. 6.11d).

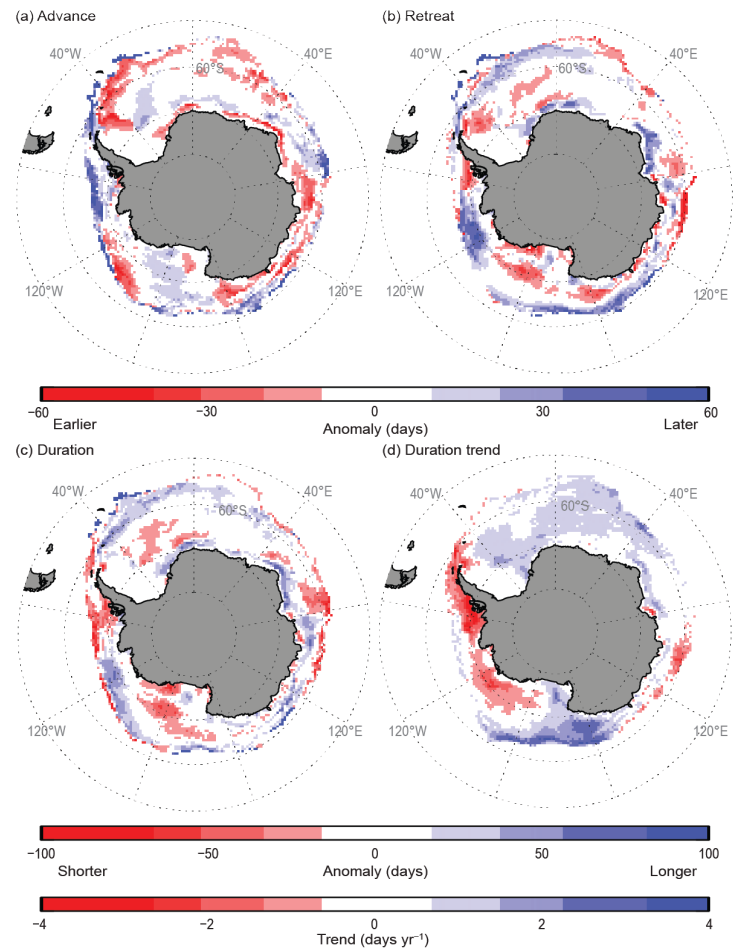


Fig. 6.11. Seasonal sea ice anomalies (days) in 2020 of (a) advance and (b) retreat; (c) total duration and (d) duration trend (Stammerjohn et al. 2008). Both the climatology (for computing the anomalies) and trend are based on 1981/82 to 2010/11 data (Cavaliere et al. 1996, updated yearly), while the 2020/21 duration-year data are from the NASA Team NRTSI dataset (Maslanik and Stroeve 1999).

Sidebar 6.2. “Disruption events” and large shifts in sea ice anomalies: a tropical–high latitude tango—P. REID, R. FOGT, AND X. YUAN

While there are some quite distinct cryospheric processes and features that influence Antarctic weather and climate variability (e.g., atmosphere–ocean–sea ice–ice sheet interactions, shallow stable atmospheric boundary layers, and strong horizontal atmospheric moisture gradients), the sensitivity of the Antarctic climate to tropical variability underscores the important role of strong tropical teleconnections (e.g., Yuan et al. 2018). On a year-to-year basis, variability in the tropics, driven by interactions between the ocean and atmosphere, often results in large-scale modes of climate variability such as the El Niño–Southern Oscillation (ENSO), Indian Ocean dipole, Atlantic Multidecadal Oscillation, and Madden-Julian Oscillation (MJO). The original tropical signal may manifest itself in the form of atmospheric Rossby waves that travel southward and influence the position and strength of the upper-tropospheric jet streams through poleward fluxes of momentum and heat (Yuan et al. 2018). In turn, the anomalous position of the jet streams alters the position of cyclogenesis around Antarctica (Riehl and Teweles 1953; Vederman 1954; Raphael et al. 2016), most frequently changing the depth of the atmospheric phenomenon known as the Amundsen Sea Low (ASL; Li et al. 2015; Raphael et al. 2016; Yuan et al. 2018) and the strength of the westerly winds and the Southern Annular Mode (SAM; Fogt and Marshall 2020). Variations in the convective zone of the southeast Pacific (the South Pacific Convergence Zone) also alter West Antarctic climate through Rossby wave interaction (Clem et al. 2020b; Stammerjohn and Scambos 2020).

The high-latitude atmospheric response to tropical teleconnections, as described above, can induce large sea ice extent (SIE) anomalies, particularly if local atmospheric phenomena (e.g., ASL, SAM) amplify or abruptly change the regional distribution of the SIE anomaly. In some cases the anomalous SIE response may be considered a “disruption event” (e.g., Hirota et al. 2018) such that the SIE anomaly is not only at, or near, record-breaking magnitude, but also exhibits a strong shift in sign. To further exemplify what we mean by disruption events, we give two examples below.

As discussed in section 6f, net SIE in 2020 increased from generally below average early in the year to, quite rapidly (1–2 weeks), above average from August through mid-December (Fig. SB6.2, red line). The main contributor to this sudden increase in SIE was the development of a strong ASL in August that continued to deepen in September (Figs. SB6.3b,c). The strong ASL resulted from Rossby wave activity associated with a developing La Niña (and

associated changes in the Walker Circulation, as measured by the Southern Oscillation Index), which is typical for this phase of ENSO (Yuan 2004). The result of the strong ASL was above-average SIE within the Ross Sea and below-average SIE in the Amundsen–Bellinghousen Seas region (Figs. SB6.3b, 6.10b; Stammerjohn et al. 2008). The relationship between the variability of the ASL and the resultant sea ice distribution is complex (Raphael et al. 2016) and is discussed in more detail in section 6f with respect to 2020. However, the timing of the SIE anomaly reversal is also important: August, when the La Niña began to intensify, is toward the end of the sea ice advance season and, as described in section 6f, led to persistently positive net SIE anomalies through mid-December 2020 (Fig. SB6.2, red line). This SIE anomaly reversal in early August 2020 is particularly noteworthy as a disruption event because prior to 2020, net circumpolar SIE had been anomalously and persistently negative for more than 3 years (since the austral spring of 2016; Reid et al. 2020), thus it took an event of this scale to shift the net SIE anomaly from persistently negative to positive (for at least four consecutive months).

When a disruption event happens early in the sea ice advance season (or conversely later in the ice retreat season), the magnitude of the SIE anomaly reversal can be even larger, as occurred in 1980. In contrast to 2020, a positive anomaly of the ASL—a high-latitude blocking high—developed during early 1980

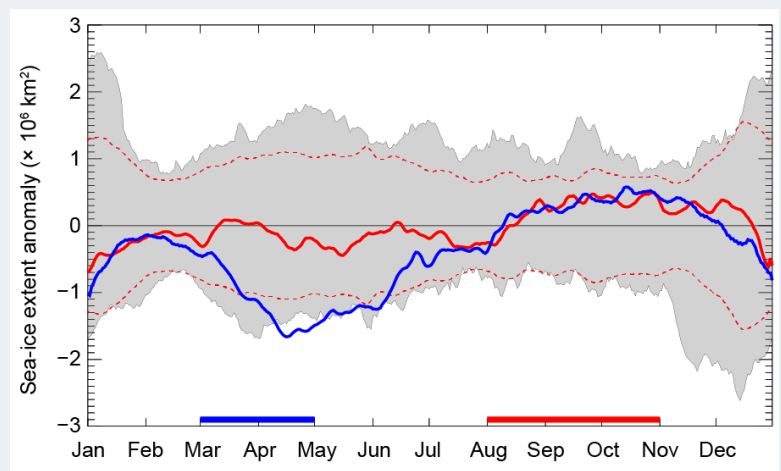


Fig. SB6.2. Time series of net (total) sea ice extent anomaly ($\times 10^6 \text{ km}^2$; 1981–2010 base period) for 2020 (red line) and 1980 (blue line). The gray shading represents historical (1981–2020) SIE anomalies; dotted red contours are the ± 1 std. dev. The blue horizontal line represents the period of high-latitude blocking high in 1980. The red horizontal line represents the period of deep Amundsen Sea Low in 2020.

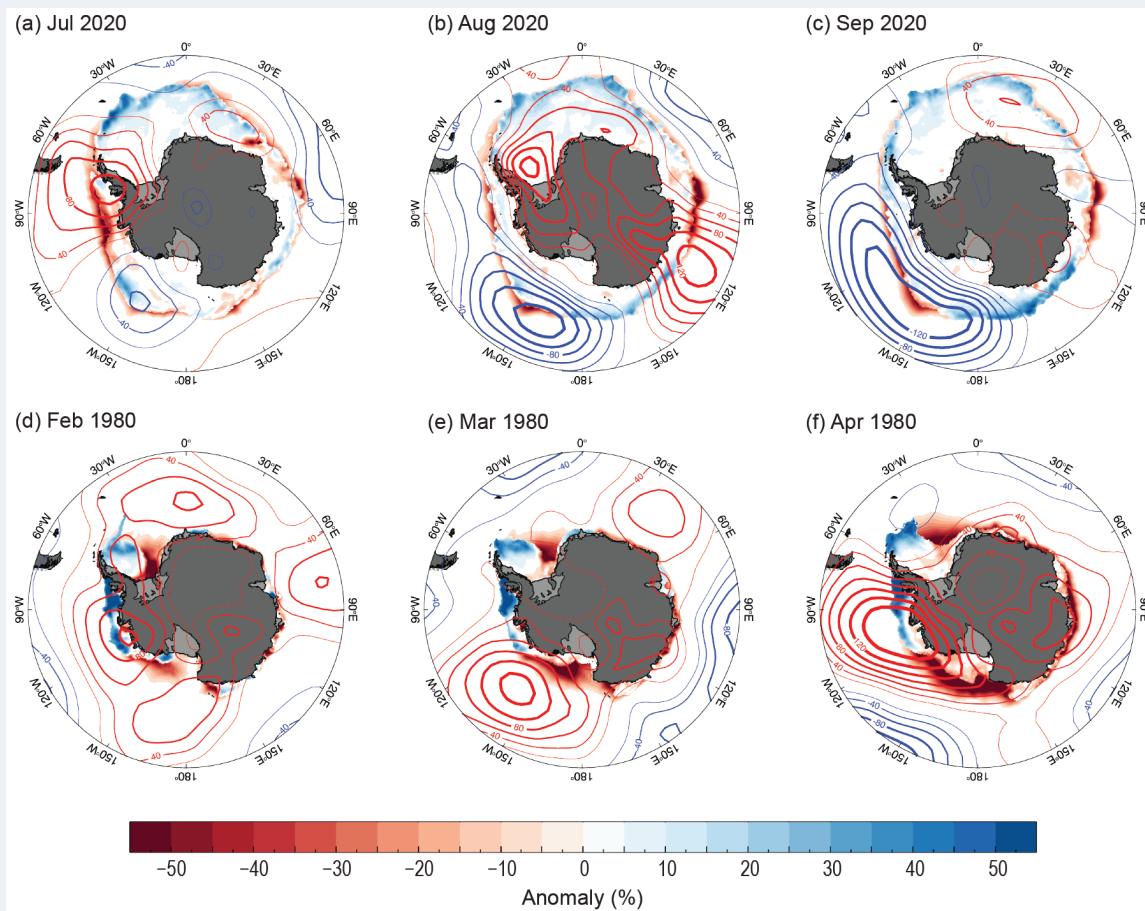


Fig. SB6.3. Anomalies of monthly mean sea ice concentration (%) and 850-hPa geopotential height (hPa) over Antarctica for (a) Jul 2020, (b) Aug 2020, (c) Sep 2020, (d) Feb 1980, (e) Mar 1980, and (f) Apr 1980. Anomalies are based on the 1981–2010 climatology.

(Figs. SB6.3d–f) and produced a strong but opposite response in sea ice distribution, e.g., strongly negative versus positive SIE anomalies in the Ross Sea. This response was associated with a weakening El Niño combined with MJO activity in the west and central Pacific (based on the MJO index of Wheeler and Hendon 2004) 200-hPa zonal wind, and satellite-observed outgoing longwave radiation (OLR). In this region (west/central Pacific), MJO activity is often associated with a high-latitude blocking high within the central and eastern Ross Sea (Lee and Seo 2019). The response in sea ice distribution was strong, with the net SIE reaching record daily lows (Fig. SB6.2, blue line). Many of those daily lows that occurred in April and early May 1980 are still records, even 40 years later. During March and April 1980, SIE expanded by only $\sim 4.3 \times 10^6 \text{ km}^2$, the lowest rate of expansion on record for those months and over 2 standard deviations below average ($\sim 5.4 \times 10^6 \text{ km}^2$). The record daily low SIE in late April to early May 1980 was largely the result of strong northerly winds focused on the Ross Sea (Figs. SB6.3e,f), i.e., on-ice winds that kept the ice edge southward. Elsewhere, weakened westerly winds in association with a strong negative

SAM index also contributed to negative SIE anomalies through weakened Ekman transport of the ice edge northward. By June, however, the SIE began to rapidly expand in association with strengthened westerly winds and increased Ekman transport northward; these favorable conditions were sustained through mid-December, promoting positive SIE anomalies from mid-August to mid-December 1980 (Fig. SB6.2).

There is a wide body of scientific literature examining how the tropics modulate Antarctic SIE and when amplified locally, the SIE anomalous response can be extreme in terms of magnitude and sign reversal (and thus a disruption event). But equally important is how Antarctic sea ice variability, particularly during disruption events, might influence extrapolar regions of the Southern Hemisphere, a topic much less studied. In the high wind and wave environment of the Southern Ocean, sea ice amplifies variability from both the atmosphere and ocean through its constraint on atmosphere–ocean fluxes. The 2 years discussed above, 1980 and 2020, are examples of amplified Antarctic SIE variability, and within that context, the following questions arise:

1. Does the regional distribution of sea ice play a passive or active role in modulating the tropical–high latitude connection, particularly during disruption events?
2. Conversely, what impact does the regional distribution of sea ice have on the midlatitude and tropical weather/climate systems?

The second question has been examined on a climate-scale scenario for both the Arctic and Antarctic, most recently using fully coupled global models (England et al. 2020). This work suggests that ice loss in the Antarctic region causes an oceanic and atmospheric northward heat transport, with the ocean

signal dominating on climate time scales of a century or more. For the Arctic, coupling an ice–ocean model to an atmospheric model has shown an improvement in tropical cyclone forecast guidance (Smith et al. 2018).

In posing these questions we must remember that the tropical–high latitude interaction is not the only forcing influencing sea ice distributions. Other factors such as stratospheric ozone and Southern Ocean variability also play significant roles (NAS 2017). While much progress has been made toward better understanding the drivers of Antarctic climate variations, many exciting research opportunities still remain.

g. Southern Ocean—V. Tamsitt, S. Bushinsky, Z. Li, M. du Plessis, A. Foppert, S. Gille, S. Rintoul, E. Shadwick, A. Silvano, A. Sutton, S. Swart, B. Tilbrook, and N. L. Williams

The Southern Ocean (SO) plays a unique role in the climate system and is responsible for 40% of oceanic anthropogenic carbon dioxide (CO₂) uptake and 75% of the ocean's uptake of heat from the atmosphere (Frölicher et al. 2015). The relatively recent increases in deployments of biogeochemical floats (Claustre et al. 2020), Saildrone Uncrewed Surface Vehicles (USVs; Sutton et al. 2021), and Deep Argo (Roemmich et al. 2019) have provided novel insights into seasonal and interannual variability in SO properties and fluxes. Here, we present 2020 anomalies of SO air–sea heat and CO₂ fluxes and show recent changes in mixed layer (ML) and Antarctic Bottom Water (AABW) properties.

1) Air–sea heat flux

We use the ERA5 reanalysis to evaluate the annual and 1981–2010 climatological state of the surface net heat flux for the SO (all ocean data points south of 40°S, with means area-weighted; positive values indicate ocean heat gain). The SO annual mean heat flux anomalies varied between positive (maximum: 1.31 W m⁻²) and negative (minimum: -1.28 W m⁻²) values with a 5–10 year period (Fig. 6.12a). The 2020 SO annual heat flux anomaly was moderately positive (+0.20 ± 0.12 W m⁻²) and followed other positive heat flux anomalies over 2014–19 (excepting 2018). However, we note that the 2020 positive SO annual heat flux anomaly is an average of both large positive and negative regional anomalies. The multi-year (1979–2020) mean heat flux anomaly was -0.01 W m⁻² compared to the 1981–2010 climatology, emphasizing that the 1981–2010 time series begins and ends with a phase of negative heat flux anomalies. We note that the time series of net heat flux anomalies differs in the magnitude and range from that presented in *State of the Climate in 2019* (Queste et al. 2020), which is due to a switch in reanalysis products from NCEP to ERA5, as ERA5 heat fluxes were deemed more reliable (Tamsitt et al. 2020).

The SO annual mean net heat flux for 2020 and climatology show broad spatial agreement in the sign of the heat flux (Figs. 6.12b,c). Within the open ocean (40°S to the sea ice edge) and particularly within the Antarctic Circumpolar Current (ACC) domains, there was widespread heat gain in the South Atlantic and Indian Oceans, and heat loss in the South Pacific Ocean. Within the sea ice sector, heat loss was generally found nearer to the Antarctic coast, with heat gain toward the winter sea ice edge (except in portions of the Indian Ocean at 60°E, Ross Sea at 180°E, and Amundsen Sea at 120°W, where heat loss extended to the winter ice edge).

The difference between 2020 and the climatology (Fig. 6.12d) reveals mostly positive heat flux anomalies in the sea ice sector in 2020, with a mean of +0.23 ± 0.01 W m⁻², where the uncertainty is the standard error of the mean. In the open ocean (40°S to the sea ice edge), the mean heat flux anomaly was +0.19 ± 0.02 W m⁻², with the positive anomalies in the Pacific Ocean and north of

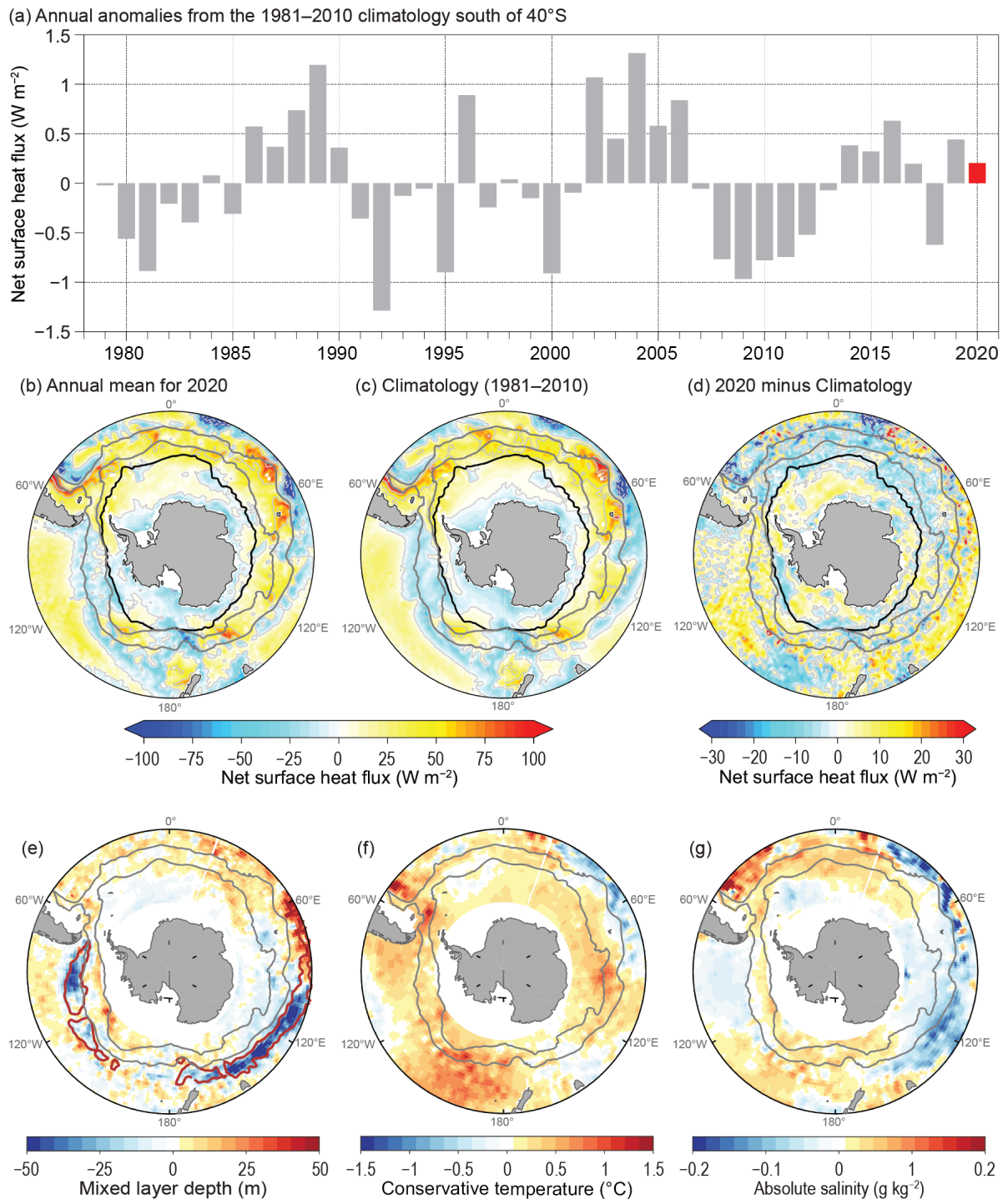


Fig. 6.12. 2020 anomalies of net air–sea heat flux and mixed layer (ML) properties. (a) Time series of ERA5 net air–sea heat flux annual mean anomalies (W m^{-2}) from the 1981–2010 mean for the entire Southern Ocean south of 40°S. The 2020 anomaly is highlighted in red. Maps of ERA5 mean net air–sea heat flux (W m^{-2}) for (b) 2020, (c) climatology (1981–2010), and (d) 2020 minus climatology. Maps of gridded Argo 2020 annual mean anomalies relative to 2004–10 mean of (e) ML depth (m), (f) ML conservative temperature (°C), and (g) ML absolute salinity (g kg^{-1}). MLD is defined using a density threshold following de Boyer Montégut et al. 2004. Gray contours in (b)–(g) show the mean position of the Subantarctic and Polar Fronts from Sokolov and Rintoul (2009). Black contours in (b)–(d) indicate the Sep 2020 mean 15% sea ice concentration from the University of Bremen AMSR2 daily 6.25-km gridded sea ice product and light gray contours in (b)–(d) are the zero net heat flux line. Red contours in (e) indicate a maximum MLD of 300 m. On all maps the outer latitude is 40°S.

the ACC outweighing the mostly negative anomalies in the Atlantic and Indian Oceans. Strong negative heat flux anomalies are attributed to the Agulhas and Falklands Western Boundary Currents, while eddy-like features between 40°S and 45°S can be identified by the large heat gain and loss anomalies, which are averaged out in the long-term mean.

2) Mixed layer properties

Anomalies of mixed layer depth (MLD) and ML conservative temperature (i.e., temperature proportional to potential enthalpy to better represent heat content) and absolute salinity in 2020 were computed relative to the climatological (2004–10) seasonal cycle (Figs. 6.12e–g) using monthly gridded Argo data (Roemmich and Gilson 2009).

In 2020, the most significant observation is the shallower MLs (Fig. 6.12e) occurring in the deepest wintertime ML regions, particularly in the southeast Pacific and southeast Indian Subantarctic Mode Water (SAMW) formation regions, where the annual mean MLD was >50 m shallower than climatology. This contrasts with a deeper ML in the central Indian SAMW formation region. The negative MLD anomaly corresponds to the location of positive air–sea heat flux anomaly (i.e., weaker heat loss; Fig. 6.12d). As a consequence of the anomalous heat gain, a warmer ML was found in the Pacific and southeast Indian sectors, while a colder ML was observed in the central Indian Ocean (Fig. 6.12f). A less saline ML was also observed in the warming ML region of the southeast Indian and southwest Pacific Oceans, contributing to the ML shoaling. Anomalies in the MLD induce anomalies in the subduction and volume of SAMW (Sallée et al. 2010; Li et al. 2021) and thus anomalies in the oceanic uptake of anthropogenic heat and carbon.

3) Air–sea CO₂ flux

Recent technological advancements in making direct measurements of air and surface seawater *p*CO₂ and wind speed autonomously from USV have reduced observational uncertainties in the Southern Ocean carbon budget by targeting gaps in the observing system (Sabine et al. 2020). The novel USV data, an example of which is shown for 2019 (Fig. 6.13a), can be used to estimate potential error in different CO₂ flux estimates. Once the air–sea gradient in CO₂ is determined, different satellite-based wind speed products and sampling frequencies have the largest impact on CO₂ flux uncertainty with biases ranging from –4% to +20% (Sutton et al. 2021).

Biogeochemical profiling floats deployed by the Southern Ocean Carbon and Climate Observations and Modeling project (SOCCOM) also complement the shipboard underway measurements that underpin air–sea CO₂ flux estimates (Figs. 6.13b–d). Unlike earlier studies, USV-, ship-, and float-based estimates of CO₂ flux were found to be in good agreement in 2019 (Sutton et al. 2021). Float-based flux estimates have greater uncertainty compared to ship and USV estimates, yet yield new information about seasonal cycles and interannual variations. Nonetheless, anomalously strong winter outgassing in the Antarctic Zone (AZ), the area between the Polar Front and the seasonally ice-covered ocean (see also Fig. 6.13a), was consistently indicated (Fig. 6.13d), both as estimated from floats (Gray et al. 2018) and float-derived products (Bushinsky et al. 2019) for 2014–17 and for the 2014–20 float-only AZ annual average flux ($+0.18 \pm 0.11$ Pg C yr⁻¹) relative to the 1982–2010 mean ship-derived AZ fluxes (e.g., Landschützer et al. 2016, $+0.01 \pm 0.035$ Pg C yr⁻¹; Rödenbeck et al. 2013, $+0.01 \pm 0.038$ Pg C yr⁻¹). These float-estimated anomalies reinforce the need to utilize all ship-, USV-, and float-based *p*CO₂ measurements in order to form a fully resolved seasonal, spatial, and interannual picture of SO carbon uptake.

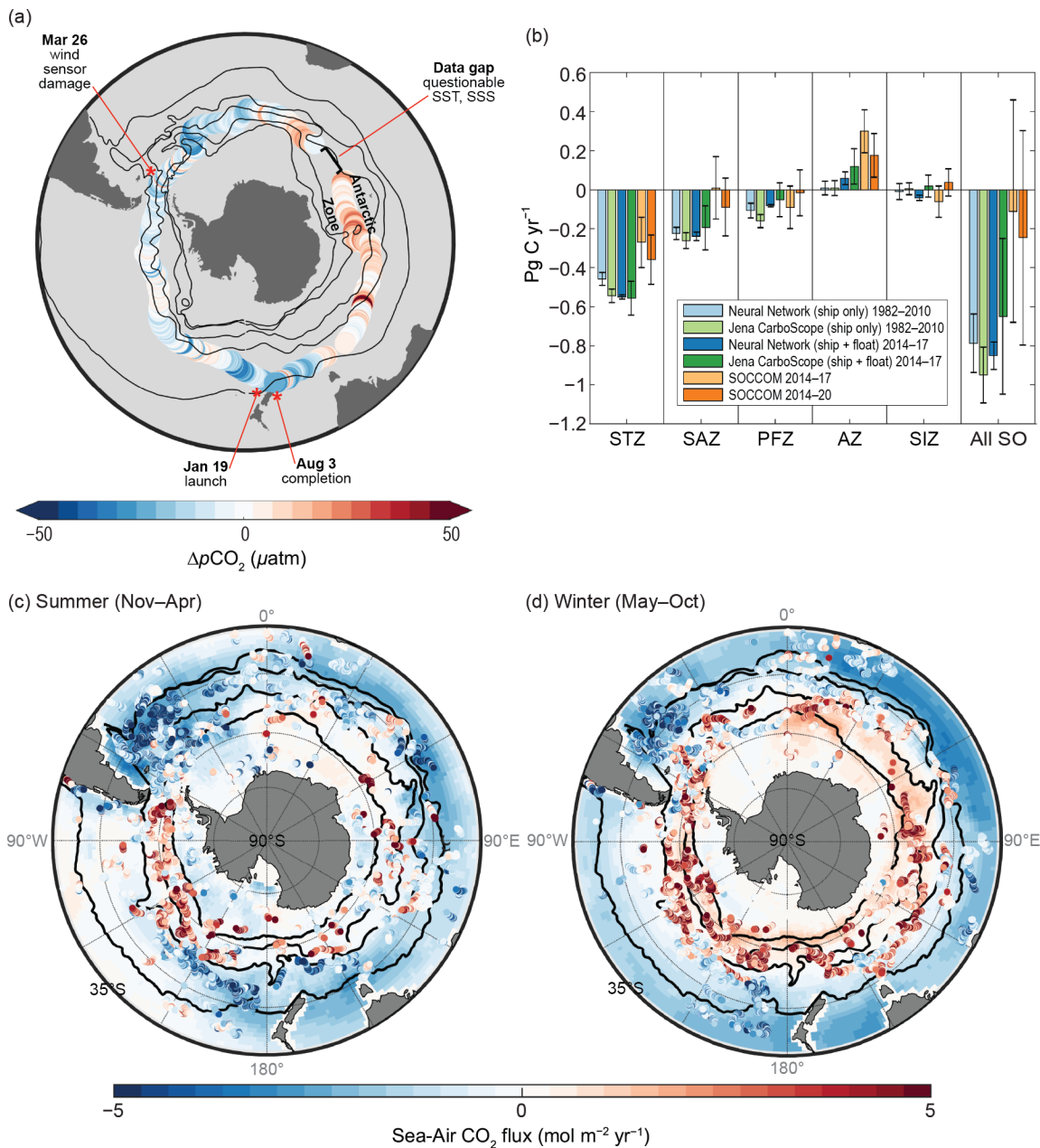


Fig. 6.13. Sea-air fluxes of CO_2 . (a) Uncrewed Surface Vehicles-measured $\Delta p\text{CO}_2$ (seawater-air; μatm) in the Southern Ocean in 2019. Black lines indicate climatological locations of the major fronts as described in Sutton et al. (2021). (b) Annual mean fluxes (Pg C yr^{-1}) for long-term ship-derived averages, 2014–17 combined ship and float averages, and float-derived 2014–17 estimates from Bushinsky et al. (2019), and float-derived estimates from 2014–20. A 2014–20 average for float estimates is presented instead of 2020 data alone as year-to-year variations in float data coverage make unmapped interannual variability difficult to determine at current float densities. (c) Summer (Nov–Apr) fluxes ($\text{mol m}^{-2} \text{yr}^{-1}$) showing 1982–2010 mean (base map) from Landschützer et al. (2016) and float-derived instantaneous fluxes from 2014–20 SOCCOM biogeochemical profiling floats (colored circles). Note the difference in temporal averaging between the base map (6-month) and float data (6-hourly). Black lines represent the Subtropical Front, Subantarctic Front, Polar Front, and seasonal ice extent (Gray et al. 2018), from north to south, delineating the Subtropical Zone, Subantarctic Zone, Polar-Frontal Zone, Antarctic Zone, and Seasonal Ice Zone. (d) Same as (c) but for winter (May–Oct) months. In all plots, positive is a flux to the atmosphere.

4) *Recent recovery of Antarctic Bottom Water formation*

Observations during the past half century showed a sustained warming, freshening, and decrease in volume of AABW (Johnson 2008; Purkey and Johnson 2013; van Wijk and Rintoul 2014; Menezes et al. 2017; Aoki et al. 2020). These changes have been linked to increased melting of the Antarctic Ice Sheet (AIS; Jacobs and Giulivi 2010; Jullion et al. 2013).

More recent ship and Deep Argo observations have revealed a rebound in AABW properties. AABW volume and salinity in the Ross Sea have increased since 2014 (Castagno et al. 2019; Silvano et al. 2020; Thomas et al. 2020; Bowen et al. 2021), and in the Weddell Sea AABW volume increased between 2014 and 2018 (Abrahamsen et al. 2019). In the Ross Sea, renewal of AABW formation has been attributed to an unusual combination of positive Southern Annular Mode and extreme El Niño conditions between 2015 and 2018 that produced anomalies in coastal winds that in turn drove increased sea ice formation, shelf water salinity increases, and a larger volume of dense AABW (Silvano et al. 2020). In the Weddell Sea, the causes of the recent AABW rebound are less clear (Abrahamsen et al. 2019; Gordon et al. 2020). While the projected increase in melt of the AIS will likely continue to drive a reduction in AABW formation, recent reversals of this trend underscore the sensitivity of the coupled ocean–cryosphere system to climate modes, teleconnections, and episodic events (e.g., iceberg calving; Shadwick et al. 2013).

h. 2020 Antarctic ozone hole—N. Kramarova, P. A. Newman, E. R. Nash, S. E. Strahan, C. S. Long, B. Johnson, M. Pitts, M. L. Santee, I. Petropavlovskikh, L. Coy, J. de Laat, G. H. Bernhard, S. Stierle, and K. Lakkala

The 2020 ozone hole was the 12th largest since the start of the NASA satellite observational record in 1979 at 23.5 Mkm² (the average area for 7 September to 13 October), with a minimum total ozone column of 94 Dobson units (DU). The 2020 austral spring was marked by a lack of planetary wave activity that resulted in a cold and stable polar stratospheric vortex, creating favorable conditions for ozone depletion. Due to the weaker-than-usual planetary-scale wave activity from September to December—waves that propagate from the troposphere into the stratosphere that force warming of the stratosphere and deceleration of the westerly polar night jet—the winter-to-summer circulation transition was delayed by several weeks, leading to the longest-lived ozone hole in the observational record. Record low ozone values in late austral spring and early summer led to unusually high levels of ultraviolet (UV) radiation in the Antarctic region (the area nominally south of 60°S).

Persistently low temperatures were observed in the Antarctic lower stratospheric vortex during winter and spring 2020 (Fig. 6.14a). Low temperatures supported formation of polar stratospheric clouds (PSCs), whose combined volume was above average in July and August (Fig. 6.14b). These clouds provide surfaces for heterogeneous chemical reactions that release chlorine (Cl₂), which is converted to active, ozone-destroying chlorine species after sunlight returns to polar latitudes in late August and September. In September, the key month for ozone depletion, vortex-averaged temperatures on the 440 K isentropic surface (~60 hPa or ~19 km) were consistently near or below the 2005–18 average, sustaining the PSC volume at near-average levels (Figs. 6.14a,b). Chlorine monoxide (ClO) concentrations (Fig. 6.14c) were near average until mid-September and above average in early October, similar to 2015. The 2020 vortex-mean ozone concentrations on the 440 K isentropic surface were close to average throughout the entire season (Fig. 6.14d) and reached a minimum in early October. The ozone hole area—the area with the total ozone column below 220 DU—peaked on 20 September (Fig. 6.14e). The partial ozone column between 12 km and 20 km derived from ozone sonde observations at the South Pole (Fig. 6.14f) declined rapidly in September and measured 6.1 DU on 15 October, the third lowest since sonde observations began in 1986. The lowest 2020 total ozone column of 94 DU was observed on 6 October (Fig. 6.14g).

In most years, planetary wave activity increases in September and October, decelerating the circumpolar winds and increasing lower stratospheric temperatures. This wave activity forces poleward and downward transport of ozone-rich air to the Antarctic lower stratosphere. This strong austral spring advection replenishes ozone in the depleted Antarctic region during the

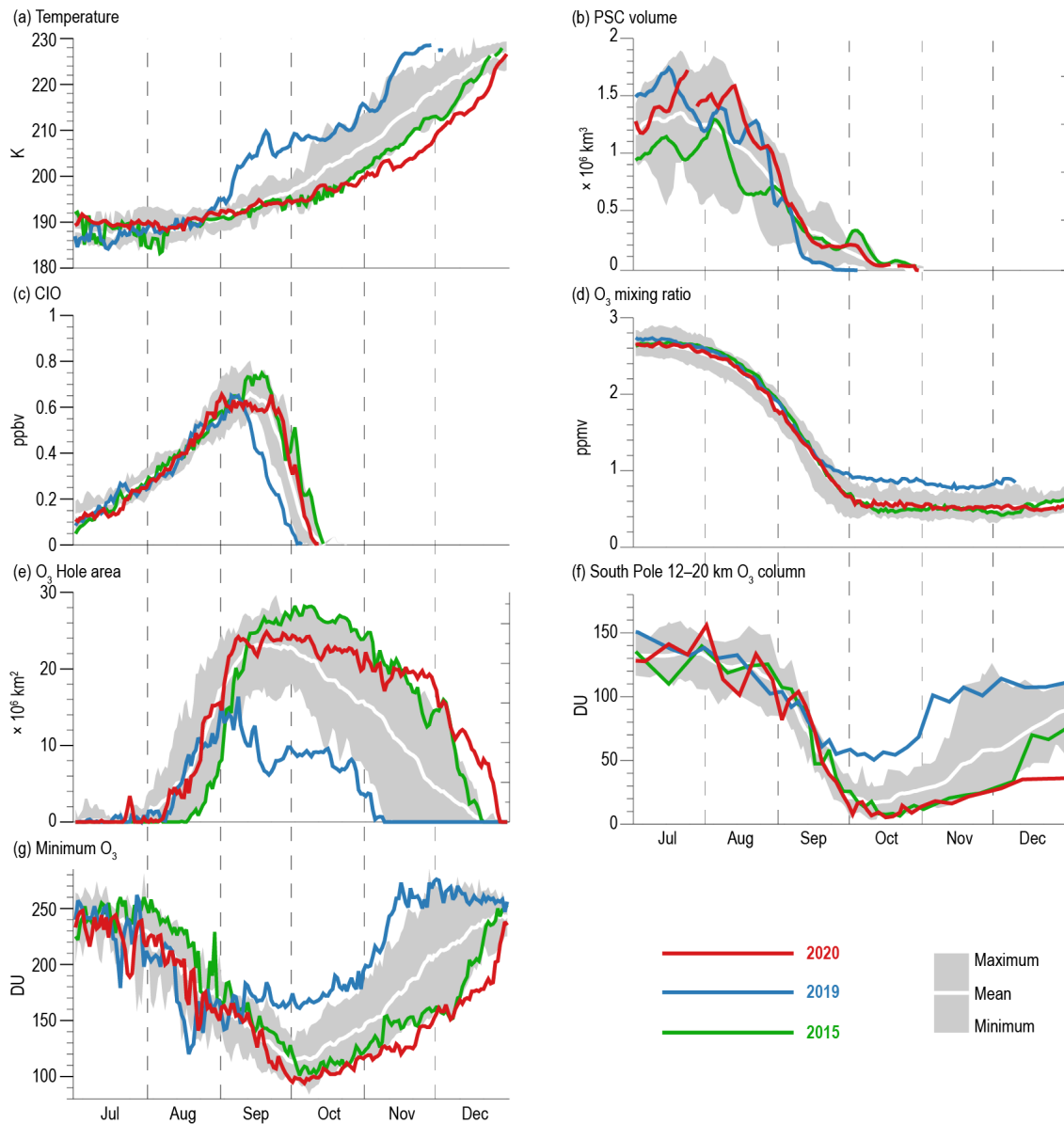


Fig. 6.14. Antarctic values of (a) vortex-averaged MERRA-2 temperature (K), (b) CALIPSO PSC volume ($\times 10^6 \text{ km}^3$; updated from Pitts et al. 2018), (c), (d) vortex-averaged ClO (ppbv) and O_3 (ppmv) measured by the *Aura* Microwave Limb Sounder (MLS; updated from Manney et al. 2011), (e) Antarctic ozone hole area ($\times 10^6 \text{ km}^2$; area with ozone total column less than 220 Dobson units [DU]) measured by the *Aura* Ozone Monitoring Instrument (OMI) and Suomi National Polar-orbiting Partnership/Ozone Mapping and Profiler (SNPP OMPS), (f) lower stratospheric ozone column (12–20 km, DU) based on sonde measurements at South Pole, and (g) minimum total column ozone (DU) over $60^\circ\text{--}90^\circ\text{S}$ from OMI/OMPS. MERRA-2 temperature and MLS averages are made inside the polar vortex on the 440 K potential temperature surface ($\sim 19 \text{ km}$ or 60 hPa). Gray shading shows the range of daily Antarctic values for 2005 (for all but (b), which starts in 2006) through 2018. The white curve indicates the 2005–18 mean.

October–November period. Conditions in 2020 diverged from this typical behavior. Wave activity was weaker than average in August and September and at record low levels in October and November, resulting in a cold and stable polar vortex that persisted through December. Starting in late October, the Antarctic lower stratosphere saw a number of low-temperature records (Fig. 6.14a). The November-mean temperature at 50 hPa hit a record low of 213.2 K, 12.9 K below the November mean for the entire observational period (1980–2019).

The weak wave activity throughout the austral spring slowed the winter-to-summer transition, resulting in the longest-lived ozone hole in the observational record. The minimum total column ozone (Fig. 6.14g) reached record low values in November and December 2020. The 12–20 km ozone

column values at the South Pole were consistently below average since late September, breaking a number of daily records from late-October to December (Fig. 6.14f). Recent model-based studies (e.g., Müller et al. 2018) demonstrated that when the vortex remains cold and stable, as it did in 2020, near-complete lower stratospheric ozone destruction can still occur at the current levels of chlorine and bromine, even though they are 12.4% lower than their peak in 2000.

Monthly mean ozone hole areas in November and December 2020 were the largest on record at 19.5 Mkm² and 8.9 Mkm², respectively; in most other years the ozone hole disappeared by December. Similarly, the year 2015 exhibited weak wave activity that led to a persistently large hole and low ozone minima in October–December (Nash et al. 2016; green lines in Fig. 6.14). In both years, ozone depletion ceased by mid-October (Fig. 6.14d) because the volume of PSCs and ClO concentration dropped to near zero (Figs. 6.14b,c). Ozone column values (Figs. 6.14f,g) then remained seasonally low for the rest of the year due to the stable vortex and lack of poleward and downward transports of ozone-rich air.

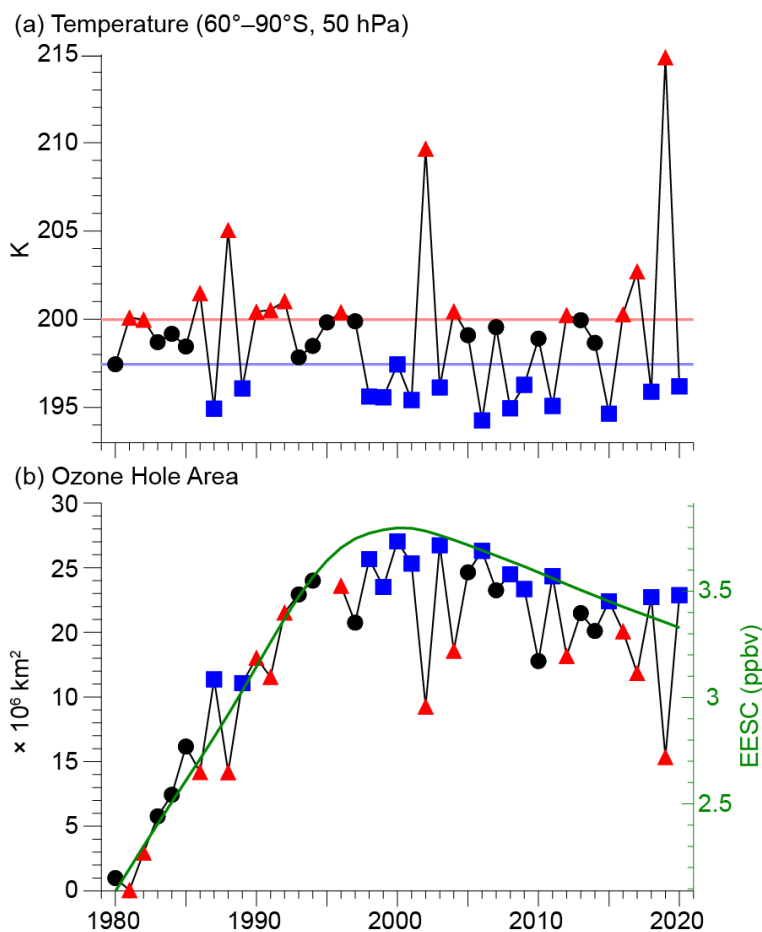


Fig. 6.15. (a) MERRA-2 50-hPa Sep mean temperature (K) averaged over 60°–90°S and (b) Sep mean Antarctic ozone hole area ($\times 10^6$ km²). Years with temperatures in the lowest (highest) third are shown as blue squares (red triangles). The horizontal blue and red lines indicate temperature levels with ± 1 std. dev. from the 1980–2020 mean (33rd and 66th percentiles). The green curve (and right vertical axis) in (b) shows the NASA-estimated EESC level in the Antarctic lower stratosphere modeled with the assumption of a 5.2 mean age of air (Newman et al. 2007). Ozone data in (b) for 1979–1992 are from the TOMS Nimbus-7, 1993–94 are from TOMS Meteor-3, 1996–2004 are from Earth Probe TOMS, 2005–15 are from *Aura* OMI, and 2016–20 are from SNPP OMPS. There were no satellite total ozone observations for 1995.

The significant ozone loss in 2020 represents a dramatic turnabout from the 2019 ozone depletion season, when a stratospheric warming event in September terminated ozone loss cycles and ended depletion early. Lower stratospheric temperatures in 2019 increased in mid-August, and the September-mean temperature was 16 K above the long-term average (blue line in Fig. 6.14a). The ClO concentrations rapidly declined in early September, and ozone levels were 13%–55% above the average in mid-September–October 2019 (blue lines in Figs. 6.14d,f,g). The 2019 warming event also enabled transport of ozone into the polar region, reducing the severity of the ozone hole, which grew to only 16.4 Mkm² in early September and vanished by early November (Fig. 6.14e).

September is the most critical month for ozone depletion (Solomon et al. 2016; Strahan et al. 2019). In this month, polar vortex temperatures are typically low and less variable than in October, and sunlight returns to polar latitudes, activating photochemical reactions that catalytically destroy ozone. The ozone hole area in September (Fig. 6.15b) is controlled by two main factors: stratospheric chlorine and bromine loading and meteorological variability. To estimate the concentration of human-produced and natural chlorine and bromine compounds in the stratosphere, we use a metric called effective equivalent stratospheric chlorine (EESC; Newman et al. 2007). The stratospheric EESC concentration maximum was reached around 2000; it declined

thereafter due to actions prompted by the 1987 Montreal Protocol and following amendments. The 2020 EESC levels are 12.4% below the peak (green line in Fig. 6.15b).

Year-to-year variations in the lower stratospheric temperature (Fig. 6.15a) also affect the severity of ozone depletion. The area of the ozone hole is larger in colder years and smaller in warmer years. To isolate the effects of declining EESC on ozone recovery, we focus on years with similarly cold meteorological conditions (blue points in Fig. 6.15). We estimate that EESC has declined by 469 ppt, from 3797 ppt to 3328 ppt, since 2000. Strahan et al. (2014) derived a linear relationship of 125 ppt EESC Mkm^{-2} between the observed ozone hole area and EESC during the coldest years. Therefore, we expect the hole area to decline at a long-term average rate of $0.19 \text{ Mkm}^2 \text{ yr}^{-1}$. Using the blue points in Fig. 6.15b that identify years with September lower stratospheric temperatures at least 1 standard deviation below the long-term mean, we calculate a downward trend in the September average ozone hole area of $0.21 \pm 0.11 \text{ Mkm}^2 \text{ yr}^{-1}$ since 2000, in good agreement with the expected trend. These results are consistent with the emergence of ozone recovery due to the Montreal Protocol despite large interannual fluctuations in the stratospheric dynamics over Antarctica (Solomon et al. 2016).

The persistence of the 2020 ozone hole until early austral summer resulted in record-breaking high UV radiation across the Antarctic region. Surface UV radiation depends on solar elevation, total ozone column, clouds, aerosols, and surface reflectivity (e.g., Bais et al. 2019). Ultraviolet radiation is quantified here with the UV Index (UVI), which is a measure of erythema (sunburn) UV radiation for human skin (WHO 2002). The UVI at the South Pole Station (Fig. 6.16a) and Arrival Heights, a coastal site near McMurdo research station (78°S , 167°E ; Fig. 6.16b), was consistently above the 1990–2019 average during October–December 2020 (red lines in Fig. 6.16), in sharp contrast to 2019 (blue lines in Fig. 6.16), when total ozone column values were on average 100 DU larger than in 2020.

As the sun's elevation approached its seasonal peak, the UVI at the South Pole reached 4.0 on 15 December. This value tied within the measurement uncertainty with the record highs in 1998 and 2015. At Arrival Heights, the UVI reached a new all-time record of 7.8 on 23 December, exceeding the previous record for this day by 2.5 units. At Marambio (Fig. 6.16c), a research station located on the Antarctic Peninsula, the daily maximum UVI exceeded 12 on several days in late November and early December 2020 when the ozone hole extended toward South America. The UVI exceeded 15 on 29 November and 1 December 2020. A UVI greater than 11 is considered extreme, and typically such high UVI values are only observed in the tropics or at high mountain elevations. The record high 2020 UVI values in the Antarctic region dramatically contrast with the low 2019 values (blue lines in Fig. 6.16 for UVI and Fig. 6.14 for ozone), illustrating how year-to-year dynamically driven ozone variability impacts surface UV radiation.

Despite persistently cold temperatures and a stable vortex, the ozone depletion in 2020 was not as severe as in the early 2000s, when the concentration of ozone-depleting substances was close to its maximum. The recovery of the Antarctic ozone hole, due to the Montreal Protocol, is becoming evident despite large interannual variability in stratospheric dynamics. Weaker-than-average wave activity during austral spring led to the delayed transition from the winter-to-summer circulation, sustaining low ozone values over Antarctica until late December and resulting in unusually high levels of UV radiation.

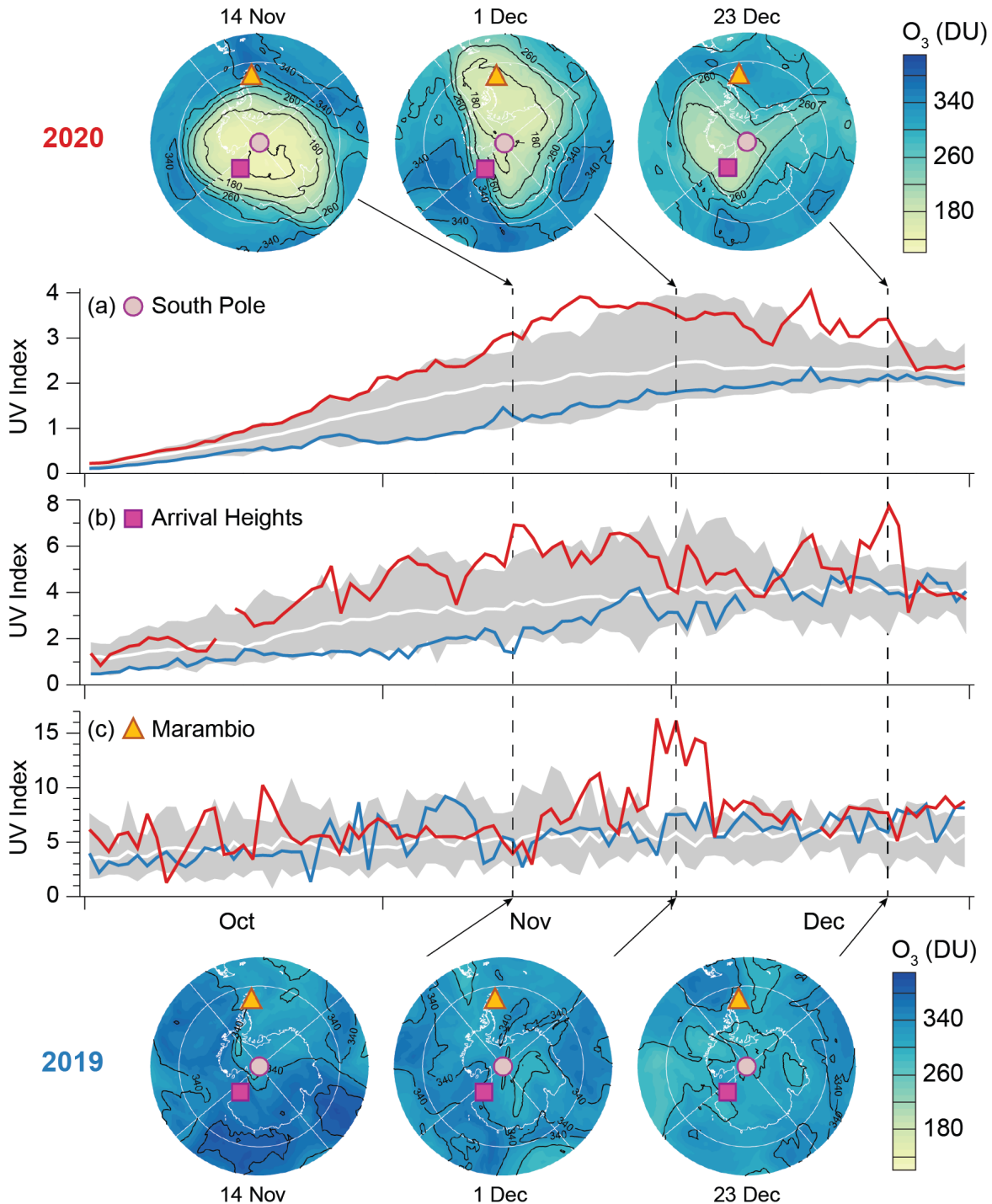


Fig. 6.16. Daily maximum UVI measured at three Antarctic stations: (a) South Pole (90°S), (b) Arrival Heights (near McMurdo Station; 78°S, 167°E), and (c) Marambio (64°S, 56°E). Colored lines show values for 2019 (blue line) and 2020 (red line), compared with each station's long-term mean (white line) and min/max range (gray shading) of similar observations between 1990 and 2018, except for Marambio, where there is a gap in data between 2011 and 2016. Data from 2019 and 2020 are preliminary and are expected to agree with final data to within $\pm 5\%$ (Aun et al. 2020; Lakkala et al. 2020). Marambio data for 2000–10 are from the Antarctic NILU-UV network (Lakkala et al. 2018). Data at South Pole and Arrival Heights up to 2009 are from the National Science Foundation's UV monitoring network (Booth et al. 1994; Bernhard et al. 2004); later data are from the NOAA Antarctic UV Monitoring Network (<https://www.esrl.noaa.gov/gmd/grad/antuv/>) and are corrected for small drifts in the calibration scale (Bernhard and Stierle 2020). Maps on the top and bottom show OMPS total ozone column values for 3 days in 2020 and 2019, respectively. Black lines indicate ozone contours.

Acknowledgments

Phil Reid and Jan Lieser were supported through the Australian Bureau of Meteorology, and Rob Massom by the Australian Antarctic Division. The work of Phil Reid and Rob Massom was also supported by the Australian Government's Australian Antarctic Partnership Program and contributes to AAS Project 4116.

Sharon Stammerjohn was supported under NSF PLR 1440435; she also thanks the Institute of Arctic and Alpine Research and the National Snow and Ice Data Center, both at the University of Colorado Boulder, for institutional and data support.

Sandra Barreira was supported by the Argentine Naval Hydrographic Service.

Ted Scambos was supported under NASA grant NNX14AM54G, the Arctic Sea Ice News and Analysis project and NSF ANT 1738992, the NSF-NERC International Thwaites Glacier Collaboration TARSAN project.

Work at the Jet Propulsion Laboratory, California Institute of Technology, was done under contract with the National Aeronautics and Space Administration (NASA). The authors would like to acknowledge Margit Aun from University of Tartu, Servicio Meteorológico Nacional (SMN) in Argentina, Spanish Agencia Estatal de Meteorología (AEMET), Argentinian Dirección Nacional del Antártico-Instituto Antártico Argentino (DNA-IAA), and Academy of Finland's projects FARPOCC and SAARA for Marambio data. Kaisa Lakkala is supported by the CHAMPS project (grant no. 329225) of the Academy of Finland under the CLIHE programme. We are indebted to the many NOAA Corps Officers and GML technical personnel who spend the winters at the South Pole Station to obtain the ongoing balloon and ground-based datasets. We also acknowledge the logistics support in Antarctica provided by the National Science Foundation Office of Polar Programs.

Veronica Tamsitt acknowledges support of CSHOR; CSHOR is a joint research Centre for Southern Hemisphere Ocean Research between QNLM and CSIRO. Air–sea heat flux data and code used in section 6g can be accessed online from doi:10.5281/zenodo.4595930. This is PMEL contribution number 5218.

Chapter 6 – Acronyms

AABW	Antarctic Bottom Water
ACC	Antarctic Circumpolar Current
AIS	Antarctic ice sheet
AMO	Atlantic Multidecadal Oscillation
AP	Antarctic Peninsula
AR	atmospheric river
ASL	Amundsen Sea Low
AWS	automated weather stations
AZ	Antarctic Zone
C3S	Copernicus Climate Change Service
CL ₂	chlorine
ClO	chlorine monoxide
CO ₂	carbon dioxide
DU	Dobson units
EAIS	East Antarctic ice sheet
EESC	equivalent stratospheric chlorine
ENSO	El Niño–Southern Oscillation
IVT	integrated water vapor transport
MJO	Madden-Julian Oscillation
ML	mixed layer
MLD	mixed layer depth
MLS	Microwave Limb Sounder
MSLP	mean sea level pressure
NSIDC	National Snow and Ice Data Center
OMI	ozone monitoring instrument
PSC	polar stratospheric cloud
SAM	Southern Annular Mode
SAMW	Subantarctic Mode Water
SAT	surface air temperature
SIE	sea ice extent
SMB	surface mass balance
SNPP OMPS	Suomi National Polar-orbiting Partnership/Ozone Mapping and Profiler
SO	Southern Ocean
SOCCOM	Southern Ocean Carbon Climate Observations and Modeling
USVs	uncrewed surface vehicles
UV	ultraviolet
UVI	ultraviolet index
w.e.	water equivalent
WAIS	West Antarctic ice sheet

References

- Abrahamsen, E. P., and Coauthors, 2019: Stabilization of dense Antarctic water supply to the Atlantic Ocean overturning circulation. *Nat. Climate Change*, **9**, 742–746, <https://doi.org/10.1038/s41558-019-0561-2>.
- Adusumilli, S., M. Fish, H. A. Fricker, and B. M. Medley, 2021: Atmospheric river precipitation contributed to rapid increases in surface height of the west Antarctic ice sheet in 2019. *Geophys. Res. Lett.*, **48**, e2020GL091076, <https://doi.org/10.1029/2020GL091076>.
- Agosta, C., and Coauthors, 2019: Estimation of the Antarctic surface mass balance using the regional climate model MAR (1979–2015) and identification of dominant processes. *Cryosphere*, **13**, 281–296, <https://doi.org/10.5194/tc-13-281-2019>.
- Aoki, S., and Coauthors, 2020: Freshening of Antarctic Bottom Water off Cape Darnley, East Antarctica. *J. Geophys. Res. Oceans*, **125**, e2020JC016374, <https://doi.org/10.1029/2020JC016374>.
- Aun, M., and Coauthors, 2020: Solar UV radiation measurements in Marambio, Antarctica, during years 2017–2019. *Atmos. Chem. Phys.*, **20**, 6037–6054, <https://doi.org/10.5194/acp-20-6037-2020>.
- Bais, A. F., G. Bernhard, R. L. McKenzie, P. J. Aucamp, P. J. Young, M. Ilyas, P. Jöckel, and M. Deushi, 2019: Ozone-climate interactions and effects on solar ultraviolet radiation. *Photochem. Photobiol. Sci.*, **18**, 602–640, <https://doi.org/10.1039/C8PP90059K>.
- Banwell, A. F., R. T. Datta, R. L. Dell, M. Moussavi, L. Brucker, G. Picard, C. A. Shuman, and L. A. Stevens, 2021: The 32-year record-high surface melt in 2019/2020 on the northern George VI Ice Shelf, Antarctic Peninsula. *Cryosphere*, **15**, 909–925, <https://doi.org/10.5194/tc-15-909-2021>.
- Barrand, N. E., D. G. Vaughan, N. Steiner, M. Tedesco, P. Kuipers Munneke, M. R. van den Broeke, and J. S. Hosking, 2013: Trends in Antarctic Peninsula surface melting conditions from observations and regional climate modeling. *J. Geophys. Res. Earth Surf.*, **118**, 315–330, <https://doi.org/10.1029/2012JF002559>.
- Bernhard, G., and S. Stierle, 2020: Trends of UV radiation in Antarctica. *Atmosphere*, **11**, 795, <https://doi.org/10.3390/atmos11080795>.
- , C. R. Booth, and J. C. Ehranjian, 2004: Version 2 data of the National Science Foundation’s ultraviolet radiation monitoring network: South Pole. *J. Geophys. Res.*, **109**, D21207, <https://doi.org/10.1029/2004JD004937>.
- Booth, C. R., T. B. Lucas, J. H. Morrow, C. S. Weiler, and P. A. Penhale, 1994: The United States National Science Foundation’s polar network for monitoring ultraviolet radiation. *Ultraviolet Radiation in Antarctica: Measurements and Biological Effects*, C. S. Weiler and P. A. Penhale, Eds., Antarctica Research Series, Vol. 62, Amer. Geophys. Union, 17–37.
- Bourassa, M. A., and Coauthors, 2013: High-latitude ocean and sea ice surface fluxes: Challenges for climate research. *Bull. Amer. Meteor. Soc.*, **94**, 403–423, <https://doi.org/10.1175/BAMS-D-11-00244.1>.
- Bowen, M. M., D. Fernandez, A. Forcen-Vazquez, A. L. Gordon, B. Huber, P. Castagno, and P. Falco, 2021: The role of tides in bottom water export from the western Ross Sea. *Sci. Rep.*, **11**, 2246, <https://doi.org/10.1038/s41598-021-81793-5>.
- Bushinsky, S. M., and Coauthors, 2019: Reassessing Southern Ocean air-sea CO₂ flux estimates with the addition of biogeochemical float observations. *Global Biogeochem. Cycles*, **33**, 1370–1388, <https://doi.org/10.1029/2019GB006176>.
- Cape, M. R., M. Vernet, P. Skvarca, S. Marinsek, T. Scambos, and E. Domack, 2015: Foehn winds link climate-driven warming to ice shelf evolution in Antarctica. *J. Geophys. Res. Atmos.*, **120**, 11 037–11 057, <https://doi.org/10.1002/2015JD023465>.
- Castagno, P., V. Capozzi, G. R. DiTullio, P. Falco, G. Fusco, S. R. Rintoul, G. Spezie, and G. Budillon, 2019: Rebound of shelf water salinity in the Ross Sea. *Nat. Commun.*, **10**, 5441, <https://doi.org/10.1038/s41467-019-13083-8>.
- Cavaliere, D. J., C. L. Parkinson, P. Gloersen, and H. J. Zwally, 1996: Sea ice concentrations from Nimbus-7 SMMR and DMSP SSM/I-SSMIS passive microwave data, version 1. NSIDC, accessed 10 February 2021, <https://doi.org/10.5067/8GQ8LZQVLOVL>.
- Claustre, H., K. S. Johnson, and Y. Takeshita, 2020: Observing the global ocean with biogeochemical-Argo. *Annu. Rev. Mar. Sci.*, **12**, 23–48, <https://doi.org/10.1146/annurev-marine-010419-010956>.
- Clem, K. R., B. R. Lintner, A. J. Broccoli, and J. R. Miller, 2019: Role of the south Pacific convergence zone in west Antarctic decadal climate variability. *Geophys. Res. Lett.*, **46**, 6900–6909, <https://doi.org/10.1029/2019GL082108>.
- , S. Barreira, R. L. Fogt, S. Colwell, L. M. Keller, M. A. Lazzara, and D. Mikolajczyk, 2020a: Atmospheric circulation and surface observations [in “State of the Climate in 2019”]. *Bull. Amer. Meteor. Soc.*, **101** (8), S293–S296, <https://doi.org/10.1175/BAMS-D-20-0090.1>.
- , R. L. Fogt, J. Turner, B. R. Lintner, G. J. Marshall, J. R. Miller, and J. A. Renwick, 2020b: Record warming at the South Pole during the past three decades. *Nat. Climate Change*, **10**, 762–770, <https://doi.org/10.1038/s41558-020-0815-z>.
- COMNAP, 2015: Sea ice challenges workshop report. COMNAP, 37 pp., <https://www.comnap.aq/publications/symposiums-workshops-reports>.
- C3S, 2017: ERA5: Fifth generation of ECMWF atmospheric reanalyses of the global climate. Copernicus Climate Change Service Climate Data Store (CDS), accessed 4 May 2018, <https://cds.climate.copernicus.eu/cdsapp#!/dataset/reanalysis-era5-single-levels-monthly-means?tab=overview>.
- de Boyer Montégut, C., G. Madec, A. S. Fischer, A. Lazar, and D. Iudicone, 2004: Mixed layer depth over the global ocean: An examination of profile data and a profile-based climatology. *J. Geophys. Res.*, **109**, C12003, <https://doi.org/10.1029/2004JC002378>.
- Depoorter, M. A., J. L. Bamber, J. A. Griggs, J. T. M. Lenaerts, S. R. M. Ligtenberg, M. R. van den Broeke, and G. Moholdt, 2013: Calving fluxes and basal melt rates of Antarctic ice shelves. *Nature*, **502**, 89–92, <https://doi.org/10.1038/nature12567>.
- England, M. R., L. M. Polvani, L. Sun, and C. Deser, 2020: Tropical climate responses to projected Arctic and Antarctic Sea ice loss. *Nat. Geosci.*, **13**, 275–281, <https://doi.org/10.1038/s41561-020-0546-9>.
- Fogt, R. L., and G. J. Marshall, 2020: The Southern Annular Mode: Variability, trends, and climate impacts across the Southern Hemisphere. *Wiley Interdiscip. Rev.: Climate Change*, **11**, 1–24, <https://doi.org/10.1002/wcc.652>.
- , D. H. Bromwich, and K. M. Hines, 2011: Understanding the SAM influence on the South Pacific ENSO teleconnection. *Climate Dyn.*, **36**, 1555–1576, <https://doi.org/10.1007/s00382-010-0905-0>.
- Forster, R. R., and Coauthors, 2014: Extensive liquid meltwater storage in firn within the Greenland ice sheet. *Nat. Geosci.*, **7**, 95–98, <https://doi.org/10.1038/ngeo2043>.
- Fountain, A. G., and J. S. Walder, 1998: Water flow through temperate glaciers. *Rev. Geophys.*, **36**, 299–328, <https://doi.org/10.1029/97RG03579>.
- Francelino, M. R. and Coauthors, 2021: WMO evaluation of two extreme high temperatures occurring in February 2020 for the Antarctic Peninsula region. *Bull. Amer. Meteor. Soc.*, <https://doi.org/10.1175/BAMS-D-21-0040.1>, in press.
- Francis, D., K. S. Mattingly, S. Lhermitte, M. Temimi, and P. Heil, 2021: Atmospheric extremes triggered the biggest calving event in more than 50 years at the Amery Ice shelf in September 2019. *Cryosphere*, **15**, 2147–2165, <https://doi.org/10.5194/tc-15-2147-2021>.
- Fricker, H. A., and A. Gardner, 2020: Recent Changes in the Antarctic Ice Sheet [in “State of the Climate in 2019”]. *Bull. Amer. Meteor. Soc.*, **101** (8), S304–S306, <https://doi.org/10.1175/BAMS-D-20-0090.1>.
- Frölicher, T. L., J. L. Sarmiento, D. J. Paynter, J. P. Dunne, J. P. Krasting, and M. Winton, 2015: Dominance of the Southern Ocean in anthropogenic carbon and heat uptake in CMIP5 models. *J. Climate*, **28**, 862–886, <https://doi.org/10.1175/JCLI-D-14-00117.1>.
- Gelaro, R., and Coauthors, 2017: The Modern-Era Retrospective Analysis for Research and Applications, version 2 (MERRA-2). *J. Climate*, **30**, 5419–5454, <https://doi.org/10.1175/JCLI-D-16-0758.1>.

- Gloersen, P., 2006: Nimbus-7 SMMR polar gridded radiances and sea ice concentrations, Version 1. Subset: 37 & 19 GHz, h-polarization, 25 km grid, Oct 1979–April 1987. NASA National Snow and Ice Data Center Distributed Active Archive Center, accessed 5 May 2020, <https://doi.org/10.5067/QOZIVYV3V9JP>.
- Gordon, A. L., B. A. Huber, and E. P. Abrahamson, 2020: Interannual variability of the outflow of Weddell Sea Bottom Water. *Geophys. Res. Lett.*, **47**, e2020GL087014, <https://doi.org/10.1029/2020GL087014>.
- Gossart, A., S. Helsen, J. T. M. Lenaerts, S. Vanden Broucke, N. P. M. van Lipzig, and N. Souverijns, 2019: An evaluation of surface climatology in state-of-the-art reanalyses over the Antarctic ice sheet. *J. Climate*, **32**, 6899–6915, <https://doi.org/10.1175/JCLI-D-19-0030.1>.
- Gray, A. R., and Coauthors, 2018: Autonomous biogeochemical floats detect significant carbon dioxide outgassing in the high-latitude Southern Ocean. *Geophys. Res. Lett.*, **45**, 9049–9057, <https://doi.org/10.1029/2018GL078013>.
- Guan, B., and D. E. Waliser, 2015: Detection of atmospheric rivers: Evaluation and application of an algorithm for global studies. *J. Geophys. Res. Atmos.*, **120**, 12 514–12 535, <https://doi.org/10.1002/2015JD024257>.
- Hall, A., and M. Visbeck, 2002: Synchronous variability in the Southern Hemisphere atmosphere, sea ice, and ocean resulting from the annular mode. *J. Climate*, **15**, 3043–3057, [https://doi.org/10.1175/1520-0442\(2002\)015<3043:SVITSH>2.0.CO;2](https://doi.org/10.1175/1520-0442(2002)015<3043:SVITSH>2.0.CO;2).
- Hirota, N., H. Shiogama, H. Akiyoshi, T. Ogura, M. Takahashi, Y. Kawatani, M. Kimoto, and M. Mori, 2018: The influences of El Niño and Arctic sea-ice on the QBO disruption in February 2016. *Climate Atmos. Sci.*, **1**, 10, <https://doi.org/10.1038/s41612-018-0020-1>.
- Jacobs, S. S., and C. F. Giulivi, 2010: Large multidecadal salinity trends near the Pacific–Antarctic continental margin. *J. Climate*, **23**, 4508–4524, <https://doi.org/10.1175/2010JCLI3284.1>.
- Johnson, G. C., 2008: Quantifying Antarctic Bottom Water and North Atlantic Deep Water volumes. *J. Geophys. Res.*, **113**, C05027, <https://doi.org/10.1029/2007JC004477>.
- Jullion, L., A. C. Naveira Garabato, M. P. Meredith, P. R. Holland, P. Courtois, and B. A. King, 2013: Decadal freshening of the Antarctic Bottom Water exported from the Weddell Sea. *J. Climate*, **26**, 8111–8125, <https://doi.org/10.1175/JCLI-D-12-00765.1>.
- Kuipers Munneke, P., S. R. M. Ligtenberg, M. R. van den Broeke, J. H. van Angelen, and R. R. Forster, 2014: Explaining the presence of perennial liquid water bodies in the firn of the Greenland ice sheet. *Geophys. Res. Lett.*, **41**, 476–483, <https://doi.org/10.1002/2013GL058389>.
- Lakkala, K., and Coauthors, 2018: UV measurements at Marambio and Ushuaia during 2000–2010. *Atmos. Chem. Phys.*, **18**, 16 019–16 031, <https://doi.org/10.5194/acp-18-16019-2018>.
- , and Coauthors, 2020: New continuous total ozone, UV, VIS and PAR measurements at Marambio, 64° S, Antarctica. *Earth Syst. Sci. Data*, **12**, 947–960, <https://doi.org/10.5194/essd-12-947-2020>.
- Landschützer, P., N. Gruber, and D. C. E. Bakker, 2016: Decadal variations and trends of the global ocean carbon sink. *Global Biogeochem. Cycles*, **30**, 1396–1417, <https://doi.org/10.1002/2015GB005359>.
- Lee, H. J., and K. H. Seo, 2019: Impact of the Madden-Julian oscillation on Antarctic sea ice and its dynamical mechanism. *Sci. Rep.*, **9**, 10761, <https://doi.org/10.1038/s41598-019-47150-3>.
- Lenaerts, J. T. M., and M. R. van den Broeke, 2012: Modeling drifting snow in Antarctica with a regional climate model: 2. Results. *J. Geophys. Res.*, **117**, D05109, <https://doi.org/10.1029/2010JD015419>.
- , E. van Meijgaard, M. R. van den Broeke, S. R. M. Ligtenberg, M. Horwath, and E. Isaksson, 2013: Recent snowfall anomalies in Dronning Maud Land, East Antarctica, in a historical and future climate perspective. *Geophys. Res. Lett.*, **40**, 2684–2688, <https://doi.org/10.1002/grl.50559>.
- , E. Keenan, M. MacLennan, and T. Gorte, 2020: Surface mass balance of the ice sheet [in “State of the Climate in 2019”]. *Bull. Amer. Meteor. Soc.*, **101** (8), S298–S300, <https://doi.org/10.1175/2020BAMSstateoftheClimate.1>.
- Lhermitte, S., and Coauthors, 2020: Damage accelerates ice shelf instability and mass loss in Amundsen Sea Embayment. *Proc. Natl. Acad. Sci. USA*, **117**, 24 735–24 741, <https://doi.org/10.1073/pnas.1912890117>.
- Li, X., E. P. Gerber, D. M. Holland, and C. Yoo, 2015: A Rossby wave bridge from the tropical Atlantic to west Antarctica. *J. Climate*, **28**, 2256–2273, <https://doi.org/10.1175/JCLI-D-14-00450.1>.
- Li, Z., M. H. England, S. Groeskamp, I. Cerovečki, and Y. Luo, 2021: The origin and fate of Subantarctic Mode Water in the Southern Ocean. *J. Phys. Oceanogr.*, <https://doi.org/10.1175/JPO-D-20-0174.1>, in press.
- Ligtenberg, S. R. M., M. M. Helsen, and M. R. van den Broeke, 2011: An improved semi-empirical model for the densification of Antarctic firn. *Cryosphere*, **5**, 809–819, <https://doi.org/10.5194/tc-5-809-2011>.
- Liu, H., L. Wang, and K. C. Jezek, 2006: Spatiotemporal variations of snowmelt in Antarctica derived from satellite scanning multichannel microwave radiometer and Special Sensor Microwave Imager data (1978–2004). *J. Geophys. Res. Earth Surf.*, **111**, F01003, <https://doi.org/10.1029/2005JF000318>.
- Liu, J., D. G. Martinson, X. Yuan, and D. Rind, 2002: Evaluating Antarctic sea ice variability and its teleconnections in global climate models. *Int. J. Climatol.*, **22**, 885–900, <https://doi.org/10.1002/joc.770>.
- MacDonell, S., F. Fernandoy, P. Villar, and A. Hammann, 2021: Stratigraphic analysis of firn cores from an Antarctic ice shelf firn aquifer. *Water*, **13**, 731, <https://doi.org/10.3390/w13050731>.
- Manney, G. L., and Coauthors, 2011: Unprecedented Arctic ozone loss in 2011. *Nature*, **478**, 469–475, <https://doi.org/10.1038/nature10556>.
- Marshall, G. J., 2003: Trends in the southern annular mode from observations and reanalyses. *J. Climate*, **16**, 4134–4143, [https://doi.org/10.1175/1520-0442\(2003\)016%3C4134:TITSAM%3E2.0.CO;2](https://doi.org/10.1175/1520-0442(2003)016%3C4134:TITSAM%3E2.0.CO;2).
- Maslanik, J., and J. Stroeve, 1999: Near-real-time DMSP SSM/I-SSMIS daily polar gridded sea ice concentrations. National Snow and Ice Data Center, accessed February 2021, <https://doi.org/10.5067/U8C09DWWX9LM>.
- Massom, R. A., and S. E. Stammerjohn, 2010: Antarctic sea ice change and variability - Physical and ecological implications. *Polar Sci.*, **4**, 149–186, <https://doi.org/10.1016/j.polar.2010.05.001>.
- , T. A. Scambos, L. G. Bennetts, P. Reid, V. A. Squire, and S. E. Stammerjohn, 2018: Antarctic ice shelf disintegration triggered by sea ice loss and ocean swell. *Nature*, **558**, 383–389, <https://doi.org/10.1038/s41586-018-0212-1>.
- Medley, B., and E. R. Thomas, 2019: Increased snowfall over the Antarctic ice sheet mitigated twentieth-century sea-level rise. *Nat. Climate Change*, **9**, 34–39, <https://doi.org/10.1038/s41558-018-0356-x>.
- Meier, W. N., H. Wilcox, M. A. Hardman, and J. S. Stewart, 2019: DMSP SSM/I-SSMIS daily polar gridded brightness temperatures, version 5. Subset: 37 & 19 GHz, h-polarization, 25 km grid, Oct 1987–April 2020. NASA National Snow and Ice Data Center Distributed Active Archive Center, accessed 11 February 2021, <https://doi.org/10.5067/QU2UYQ6T0B3P>.
- Menezes, V. V., A. M. Macdonald, and C. Schatzman, 2017: Accelerated freshening of Antarctic Bottom Water over the last decade in the Southern Indian Ocean. *Sci. Adv.*, **3**, e1601426, <https://doi.org/10.1126/sciadv.1601426>.
- Meredith, M. P., and M. A. Brandon, 2017: Oceanography and sea ice in the Southern Ocean. Sea Ice, D. N. Thomas, Ed., Wiley-Blackwell, 216–238, <https://doi.org/10.1002/9781118778371.ch8>.
- Montgomery, L., and Coauthors, 2020: Hydrologic properties of a highly permeable firn aquifer in the Wilkins Ice Shelf, Antarctica. *Geophys. Res. Lett.*, **47**, e2020GL089552, <https://doi.org/10.1029/2020GL089552>.
- Mote, T. L., 2007: Greenland surface melt trends 1973–2007: Evidence of a large increase in 2007. *Geophys. Res. Lett.*, **34**, L22507, <https://doi.org/10.1029/2007GL031976>.
- , 2014: MEASURES Greenland surface melt daily 25km EASE-Grid 2.0, Version 1. NASA National Snow and Ice Data Center Distributed Active Archive Center, accessed 10 February 2021, <https://doi.org/10.5067/MEASURES/CRYOSPHERE/nsidc-0533.001>.
- , and M. R. Anderson, 1995: Variations in snowpack melt on the Greenland ice sheet based on passive microwave measurements. *J. Glaciol.*, **41**, 51–60, <https://doi.org/10.3189/S0022143000017755>.

- Mottram, R., and Coauthors, 2020: What is the surface mass balance of Antarctica? An intercomparison of regional climate model estimates. *Cryosphere Discuss.*, <https://doi.org/10.5194/tc-2019-333>.
- Müller, R., J.-U. Groß, A. M. Zafar, S. Robrecht, and R. Lehmann, 2018: The maintenance of elevated active chlorine levels in the Antarctic lower stratosphere through HCl null cycles. *Atmos. Chem. Phys.*, **18**, 2985–2997, <https://doi.org/10.5194/acp-18-2985-2018>.
- NAS (National Academies of Sciences, Engineering, and Medicine), 2017: *Antarctic Sea Ice Variability in the Southern Ocean–Climate System: Proceedings of a Workshop*. The National Academies Press, 82 pp., <https://doi.org/10.17226/24696>.
- Nash, E., and Coauthors, 2016: Antarctic ozone hole [in “State of the Climate in 2015”]. *Bull. Amer. Meteor. Soc.*, **97** (8), S168–S172, <https://doi.org/10.1175/2016BAMSStateoftheClimate.1>.
- Newman, P., E. R. Nash, N. Kramarova, and A. Butler, 2020: Sidebar 6-1: The 2019 southern stratospheric warming [in “State of the Climate in 2019”]. *Bull. Amer. Meteor. Soc.*, **101** (8), S297–S298, <https://doi.org/10.1175/BAMS-D-20-0090.1>.
- , J. S. Daniel, D. W. Waugh, and E. R. Nash, 2007: A new formulation of Equivalent Effective Stratospheric Chlorine (EESC). *Atmos. Chem. Phys.*, **7**, 4537–4552, <https://doi.org/10.5194/acp-7-4537-2007>.
- Norwegian Polar Institute, 2018: Quantarctica v3.0, detailed basemap. www.npolar.no/quantarctica/.
- Oliva, M., F. Navarro, F. Hrbáček, A. Hernández, D. Nývlt, P. Pereira, J. Ruiz-Fernandéz, and R. Trigo, 2017: Recent regional climate cooling on the Antarctic Peninsula and associated impacts on the cryosphere. *Sci. Total Environ.*, **580**, 210–223, <https://doi.org/10.1016/j.scitotenv.2016.12.030>.
- Palm, S. P., V. Kayetha, and Y. Yang, 2018: Toward a satellite-derived climatology of blowing snow over Antarctica. *J. Geophys. Res. Atmos.*, **123**, 10301–10313, <https://doi.org/10.1029/2018JD028632>.
- Paolo, F. S., H. A. Fricker, and L. Padman, 2015: Volume loss from Antarctic ice shelves is accelerating. *Science*, **348**, 327–331, <https://doi.org/10.1126/science.aaa0940>.
- Parkinson, C. L., 2019: A 40-y record reveals gradual Antarctic sea ice increases followed by decreases at rates far exceeding the rates seen in the Arctic. *Proc. Natl. Acad. Sci. USA*, **116**, 14414–14423, <https://doi.org/10.1073/pnas.1906556116>.
- Pitts, M. C., L. R. Poole, and R. Gonzalez, 2018: Polar stratospheric cloud climatology based on CALIPSO spaceborne lidar measurements from 2006 to 2017. *Atmos. Chem. Phys.*, **18**, 10881–10913, <https://doi.org/10.5194/acp-18-10881-2018>.
- Purkey, S. G., and G. C. Johnson, 2013: Antarctic Bottom Water warming and freshening: Contributions to sea level rise, ocean freshwater budgets, and global heat gain. *J. Climate*, **26**, 6105–6122, <https://doi.org/10.1175/JCLI-D-12-00834.1>.
- Queste, B. Y., and Coauthors, 2020: Southern Ocean [in “State of the Climate in 2019”]. *Bull. Amer. Meteor. Soc.*, **101** (8), S307–S309, <https://doi.org/10.1175/BAMS-D-20-0090.1>.
- Raphael, M. N., and Coauthors, 2016: The Amundsen Sea low: Variability, change, and impact on Antarctic climate. *Bull. Amer. Meteor. Soc.*, **97**, 111–121, <https://doi.org/10.1175/BAMS-D-14-00018.1>.
- Reid, P. A., and R. A. Massom, 2015: Successive Antarctic Sea ice extent records during 2012, 2013 & 2014 [in “State of the Climate in 2014”]. *Bull. Amer. Meteor. Soc.*, **96** (7), S163–S164, <https://doi.org/10.1175/2015BAMSStateoftheClimate.1>.
- , S. Stammerjohn, R. A. Massom, S. Barreira, T. Scambos, and J. L. Lieser, 2020: Sea ice extent, concentration, and seasonality [in “State of the Climate in 2019”]. *Bull. Amer. Meteor. Soc.*, **101**, S304–S306, <https://doi.org/10.1175/BAMS-D-20-0090.1>.
- Reynolds, R. W., N. A. Rayner, T. M. Smith, D. C. Stokes, and W. Wang, 2002: An improved in situ and satellite SST analysis for climate. *J. Climate*, **15**, 1609–1625, [https://doi.org/10.1175/1520-0442\(2002\)015<1609:AIIAS>2.0.CO;2](https://doi.org/10.1175/1520-0442(2002)015<1609:AIIAS>2.0.CO;2).
- Riehl, H., and S. Teweles, 1953: A further study on the relation between the jet stream and cyclone formation. *Tellus*, **5**, 66–79, <https://doi.org/10.3402/tellusa.v5i1.8561>.
- Rignot, E., S. Jacobs, J. Mouginot, and B. Scheuchl, 2013: Ice-shelf melting around Antarctica. *Science*, **341**, 266–270, <https://doi.org/10.1126/science.1235798>.
- Roach, L. A., and Coauthors, 2020: Antarctic sea ice area in CMIP6. *Geophys. Res. Lett.*, **47**, e2019GL086729, <https://doi.org/10.1029/2019GL086729>.
- Rödenbeck, C., and Coauthors, 2013: Global surface-ocean pCO₂ and sea-air CO₂ flux variability from an observation-driven ocean mixed-layer scheme. *Ocean Sci.*, **9**, 193–216, <https://doi.org/10.5194/os-9-193-2013>.
- Roemmich, D., and J. Gilson, 2009: The 2004–2008 mean and annual cycle of temperature, salinity, and steric height in the global ocean from the Argo Program. *Prog. Oceanogr.*, **82**, 81–100, <https://doi.org/10.1016/j.pocean.2009.03.004>.
- , and Coauthors, 2019: On the future of Argo: A global, full-depth, multi-disciplinary array. *Front. Mar. Sci.*, **6**, 439, <https://doi.org/10.3389/fmars.2019.00439>.
- Rondanelli, R., B. Hatchett, J. Rutllant, D. Bozkurt, and R. Garreaud, 2019: Strongest MJO on record triggers extreme Atacama rainfall and warmth in Antarctica. *Geophys. Res. Lett.*, **46**, 3482–3491, <https://doi.org/10.1029/2018GL081475>.
- Sabine, C., and Coauthors, 2020: Evaluation of a new carbon dioxide system for autonomous surface vehicles. *J. Atmos. Oceanic Technol.*, **37**, 1305–1317, <https://doi.org/10.1175/JTECH-D-20-0010.1>.
- Sallée, J. B., K. Speer, S. R. Rintoul, and S. Wijffels, 2010: Southern Ocean thermocline ventilation. *J. Phys. Oceanogr.*, **40**, 509–529, <https://doi.org/10.1175/2009JPO4291.1>.
- Scambos, T., and Coauthors, 2009: Ice shelf disintegration by plate bending and hydro-fracture: satellite observations and model results of the 2008 Wilkins ice shelf break-ups. *Earth and Planet. Sci. Lett.*, **280**, 51–60, <https://doi.org/10.1016/j.epsl.2008.12.027>.
- Shadwick, E., and Coauthors, 2013: Glacier tongue calving reduced dense water formation and enhanced carbon uptake. *Geophys. Res. Lett.*, **40**, 904–909, <https://doi.org/10.1002/grl.50178>.
- Shepherd, A., and Coauthors, 2018: Mass balance of the Antarctic ice sheet from 1992 to 2017. *Nature*, **558**, 219–222, <https://doi.org/10.1038/s41586-018-0179-y>.
- Shepherd, A., and Coauthors, 2012: A reconciled estimate of ice-sheet mass balance. *Science*, **338**, 1183–1189, <https://doi.org/10.1126/science.1228102>.
- Silvano, A., and Coauthors, 2020: Recent recovery of Antarctic Bottom Water formation in the Ross Sea driven by climate anomalies. *Nat. Geosci.*, **13**, 780–786, <https://doi.org/10.1038/s41561-020-00655-3>.
- Smith, B., H. A. Fricker, A. S. Gardner, B. Medley, J. Nilsson, F. S. Paolo, N. Holschuh, S. Adusumilli, K. Brunt, B. Csatho, K. Harbeck, T. Markus, T. Neumann, M. R. Siegfried, and H. J. Zwally, 2020: Pervasive ice sheet mass loss reflects competing ocean and atmosphere processes. *Science*, **368**, <https://doi.org/10.1126/science.aaz5845>.
- , ———, ———, M. R. Siegfried, S. Adusumilli, B. M. Csathó, N. Holschuh, J. Nilsson, F. S. Paolo, and the ICESat-2 Science Team, 2021: ATLAS/ICESat-2 L3A Land Ice Height, Version 4, version 4. NASA National Snow and Ice Data Center Distributed Active Archive Center, accessed 20 February 2021, <https://doi.org/10.5067/ATLAS/ATL06.003>.
- Smith, G. C., and Coauthors, 2018: Impact of coupling with an ice-ocean model on global medium-range NWP forecast skill. *Mon. Wea. Rev.*, **146**, 1157–1180, <https://doi.org/10.1175/MWR-D-17-0157.1>.
- Smith, T. M., R. W. Reynolds, T. C. Peterson, and J. Lawrimore, 2008: Improvements to NOAA’s historical merged land–ocean surface temperature analysis (1880–2006). *J. Climate*, **21**, 2283–2296, <https://doi.org/10.1175/2007JCLI2100.1>.
- Sokolov, S., and S. R. Rintoul, 2009: Circumpolar structure and distribution of the Antarctic circumpolar current fronts: 1. Mean circumpolar paths. *J. Geophys. Res.*, **114**, C11018, <https://doi.org/10.1029/2008JC005108>.
- Solomon, S., D. J. Ivy, D. Kinnison, M. J. Mills, R. R. Neely, and A. Schmidt, 2016: Emergence of healing in the Antarctic ozone layer. *Science*, **353**, 269–274, <https://doi.org/10.1126/science.aae0061>.

- Stammerjohn, S., and T. Maksym, 2017: Gaining (and losing) Antarctic sea ice: Variability, trends and mechanisms. *Sea Ice*, D. N. Thomas, Ed., Wiley-Blackwell, 261–289, <https://doi.org/10.1002/9781118778371.ch10>.
- , and T. A. Scambos, 2020: Warming reaches the South Pole. *Nat. Climate Change*, **10**, 710–711, <https://doi.org/10.1038/s41558-020-0827-8>.
- , D. G. Martinson, R. C. Smith, X. Yuan, and D. Rind, 2008: Trends in Antarctic annual sea ice retreat and advance and their relation to El Niño–Southern Oscillation and Southern Annular Mode variability. *J. Geophys. Res.*, **113**, C03S90, <https://doi.org/10.1029/2007JC004269>.
- Strahan, S. E., A. R. Douglass, P. A. Newman, and S. D. Steenrod, 2014: Inorganic chlorine variability in the Antarctic vortex and implications for ozone recovery. *J. Geophys. Res. Atmos.*, **119**, 14098–14109, <https://doi.org/10.1002/2014JD022295>.
- , A. R. Douglass, and M. R. Damon, 2019: Why do Antarctic ozone recovery trends vary? *J. Geophys. Res. Atmos.*, **124**, 8837–8850, <https://doi.org/10.1029/2019JD030996>.
- Sutton, A. J., N. L. Williams, and B. Tilbrook, 2021: Constraining Southern Ocean CO₂ flux uncertainty using uncrewed surface vehicle observations. *Geophys. Res. Lett.*, **48**, e2020GL091748, <https://doi.org/10.1029/2020GL091748>.
- Tamsitt, V., I. Cerovečki, S. A. Josey, S. T. Gille, and E. Schulz, 2020: Mooring observations of air–sea heat fluxes in two Subantarctic Mode Water formation regions. *J. Climate*, **33**, 2757–2777, <https://doi.org/10.1175/JCLI-D-19-0653.1>.
- Tedesco, M., 2009: Assessment and development of snowmelt retrieval algorithms over Antarctica from K-band spaceborne brightness temperature (1979–2008). *Remote Sens. Environ.*, **113**, 979–997, <https://doi.org/10.1016/j.rse.2009.01.009>.
- Thomas, D. N., Ed., 2017: *Sea Ice*. 3rd ed. Wiley-Blackwell, 664 pp.
- Thomas, G., S. G. Purkey, D. Roemmich, A. Foppert, and S. R. Rintoul, 2020: Spatial variability of Antarctic Bottom Water in the Australian Antarctic Basin from 2018–2020 captured by Deep Argo. *Geophys. Res. Lett.*, **47**, e2020GL089467, <https://doi.org/10.1029/2020GL089467>.
- Timmermann, R., and H. H. Hellmer, 2013: Southern Ocean warming and increased ice shelf basal melting in the twenty-first and twenty-second centuries based on coupled ice–ocean finite-element modelling. *Ocean Dyn.*, **63**, 1011–1026, <https://doi.org/10.1007/s10236-013-0642-0>.
- Turner, J., and Coauthors, 2016: Absence of 21st century warming on Antarctic Peninsula consistent with natural variability. *Nature*, **535**, 411–415, <https://doi.org/10.1038/nature18645>.
- , and Coauthors, 2020: Recent decrease of summer sea ice in the Weddell Sea, Antarctica. *Geophys. Res. Lett.*, **47**, e2020GL087127, <https://doi.org/10.1029/2020GL087127>.
- van Wessem, J. M., C. R. Steger, N. Wever, and M. R. van den Broeke, 2021: An exploratory modelling study of perennial firn aquifers in the Antarctic Peninsula for the period 1979–2016. *Cryosphere*, **15**, 695–714, <https://doi.org/10.5194/tc-15-695-2021>.
- van Wijk, E. M., and S. R. Rintoul, 2014: Freshening drives contraction of Antarctic Bottom Water in the Australian Antarctic Basin. *Geophys. Res. Lett.*, **41**, 1657–1664, <https://doi.org/10.1002/2013GL058921>.
- Vederman, J., 1954: The life cycles of jet streams and extratropical cyclones. *Bull. Amer. Meteor. Soc.*, **35**, 239–244, <https://doi.org/10.1175/1520-0477-35.6-239>.
- Walsh, J. E., 1983: The role of sea ice in climatic variability: Theories and evidence. *Atmos. Ocean*, **21**, 229–242, <https://doi.org/10.1080/07055900.1983.9649166>.
- Wang, Y., and Coauthors, 2016: A comparison of Antarctic Ice Sheet surface mass balance from atmospheric climate models and in situ observations. *J. Climate*, **29**, 5317–5337, <https://doi.org/10.1175/JCLI-D-15-0642.1>.
- Watkins, A. B., and I. Simmonds, 1999: A late spring surge in the open water of the Antarctic sea ice pack. *Geophys. Res. Lett.*, **26**, 1481–1484, <https://doi.org/10.1029/1999GL900292>.
- Wheeler, M. C., and H. H. Hendon, 2004: An all-season real-time multi-variate MJO index: Development of an index for monitoring and prediction. *Mon. Wea. Rev.*, **132**, 1917–1932, [https://doi.org/10.1175/1520-0493\(2004\)132<1917:AARMMI>2.0.CO;2](https://doi.org/10.1175/1520-0493(2004)132<1917:AARMMI>2.0.CO;2).
- WHO, 2002: Global solar UV index: A practical guide. World Health Organization, 28 pp., www.who.int/uv/publications/en/GlobalUVI.pdf.
- Walker, C. C., M. K. Becker, and H. A. Fricker, 2021: A high resolution, three-dimensional view of the D-28 calving event from Amery Ice Shelf with ICESat-2 and satellite imagery. *Geophys. Res. Lett.*, **48**, <https://doi.org/https://doi.org/10.1029/2020GL091200>.
- Wiese, D. N., D.-N. Yuan, C. Boening, F. W. Landerer, and M. M. Watkins, 2019: JPL GRACE Mascon Ocean, Ice, and Hydrology Equivalent Water Height RL06 CRI Filtered Version 02, version 2. PO.DAAC, accessed 20 February 2021, <https://doi.org/10.5067/TEMSC-3JC62>.
- Wille, J. D., V. Favier, A. Dufour, I. V. Gorodetskaya, J. Turner, C. Agosta, and F. Codron, 2019: West Antarctic surface melt triggered by atmospheric rivers. *Nat. Geosci.*, **12**, 911–916, <https://doi.org/10.1038/s41561-019-0460-1>.
- Yuan, X., 2004: ENSO-related impacts on Antarctic sea ice: A synthesis of phenomenon and mechanisms. *Antarct. Sci.*, **16**, 415–425, <https://doi.org/10.1017/S0954102004002238>.
- , M. R. Kaplan, and M. A. Cane, 2018: The interconnected global climate system—a review of tropical–polar teleconnections. *J. Climate*, **31**, 5765–5792, <https://doi.org/10.1175/JCLI-D-16-0637.1>.
- Zwally, H. J., and S. Fiegles, 1994: Extent and duration of Antarctic surface melting. *J. Glaciol.*, **40**, 463–475, <https://doi.org/10.3189/S0022143000012338>.

